

AD-A243 597



PULSE SCIENCES INC.

TITAN  
CORPORATION

600 McCormick Street • San Leandro, CA 94577  
Tel: (415) 632-5100 • Telecopier: (415) 632-5300

PULSED POWER SYSTEMS DIVISION

EXPERIMENTAL STUDIES OF ELECTRON BEAM TRANSPORT  
IN STELLARATOR FOCUSING FIELDS

PSIFR-2543-01

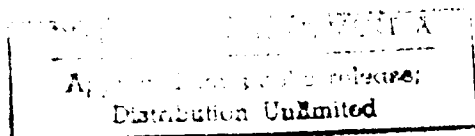


JULY 1991

WORK PERFORMED UNDER CONTRACT NO.: N00014-89-C-0227

PREPARED FOR:

OFFICE OF NAVAL RESEARCH  
ARLINGTON, VA 22217



91-17288



~~91-1112-129~~

037

**EXPERIMENTAL STUDIES OF ELECTRON BEAM TRANSPORT  
IN STELLARATOR FOCUSING FIELDS**

M.G. Tiefenback, S.D. Putnam, V.L. Bailey, Jr., J.P. Lidestri  
and J.A. Edighoffer

PSIFR-2543-01

July 1991

Work Performed Under Contract No. N00014-89-C-0227

Prepared for:

Office of Naval Research  
Arlington, VA 22217

Prepared by:

Pulse Sciences, Inc.  
600 McCormick Street  
San Leandro, CA 94577

Accession For	
NTIS GRA&I	<input checked="checked" type="checkbox"/>
DTIC TAB	<input type="checkbox"/>
Unannounced	<input type="checkbox"/>
Justification	
By <i>Pes Ltc.</i>	
Distribution/	
Availability Codes	
Dist	Avail and/or Special
<i>A-1</i>	



## TABLE OF CONTENTS

<b><u>SECTION</u></b>		<b><u>PAGE</u></b>
1.0	Introduction.....	1
2.0	Experimental Apparatus.....	3
3.0	Diode Work.....	7
4.0	Magnet Mapping.....	13
5.0	Emittance.....	14
6.0	Dispersion.....	15
7.0	Collective Phenomena.....	19
8.0	RF Pickup.....	21
9.0	Beam Loss.....	31
10.0	Summary.....	38
11.0	Suggestions for Future Investigations.....	39
	References.....	39

## ***LIST OF ILLUSTRATIONS***

<b><i>Figure</i></b>		<b><i>Page</i></b>
1	Conceptual layout of a 540-degree SLIA accelerator.....	2
2	Schematic of the experimental setup.....	5
3	Engineering drawing of the cross-section of the bend magnet.....	6
4	EGUN ray trajectories for existing diode and upgrade design.....	8
5	Measured envelope radius of the beam within the anode tube.....	11
6	Measured diode voltage and current.....	12
7	Effect of stellarator fields on beam current transmission.....	16
8	900 keV, 700 a beam transport through bend (3 kG guide field)...	16
9	Experimental beam centroid offset (3 kG guide field parallel to electron beam velocity).....	18
10	Experimental beam centroid offset (3 kG guide field anti-parallel to electron beam velocity).....	20
11	Network analyzer frequency scan of the B-dot array response.....	22
12	Bend exit B-dot signal for 325 A at a guide field strength of 1.2 kG.....	24
13	Frequency determination of B-dot probe signal using filters.....	25
14	B-dot probe signals at the entrance and exit of the bend magnet.....	27
15	Oscilloscope traces of bend exit B-dot RF power vs. time.....	28
16	Power vs. time from the data of Figures 15 (a-d).....	30
17	Network used for summing and differencing opposing B-dots.....	32
18	Sum and difference signals from opposing bend exit B-dots.....	33
19	Beam tail erosion with decreasing guide field strength.....	34
20	Beam tail erosion with increasing stellarator gradient.....	35
21	Beam tail erosion with increasing current.....	36

## *LIST OF TABLES*

<i><u>Table</u></i>		<i><u>Page</u></i>
1	Normalized beam emittances ( $\pi$ cm mrad).....	14
2	Power growth times.....	29
3	Temporal width (ns) of beam pulse passed to Faraday cup.....	37

## 1.0 INTRODUCTION

The Spiral Line Induction Accelerator (SLIA)<sup>[1]</sup> is under development as a compact accelerator potentially capable of accelerating electron beam currents up to about 10 kA to energies of many tens of MeV. The beam is guided through a few successive transits of induction acceleration cavities, as illustrated in Figure 1. The desired beam current and energies make guide field focussing a practical requirement. The open-ended geometry greatly simplifies injection and extraction of the beam with respect to a closed-orbit geometry. Strong focussing in the presence of a guide field is incorporated in the bend sections via twisted quadrupole ("stellarator") windings superimposed upon a guide field and a vertical bending field. The concept is a synthesis of ideas from linear induction accelerators, the recirculation scheme suggested by Mark Wilson<sup>[2]</sup> of NBS (now NIST), and the "stellarator" focussing proposed by Roberson, et al.<sup>[3]</sup>. Each segment of the magnetic channel need be optimized only for a relatively narrow energy range; there is no need for rapid cycling of the focussing fields. An accelerator experiment using this principle at the level of 10 kA of beam current, with an energy of approximately 10 MeV (two acceleration passes) is presently in progress to validate the focussing and dispersive characteristics of the SLIA bends and experimentally determine the consequences of off-axis acceleration of high-current beams in induction cavities prior to attempting higher energy through multiple recirculation passes. The fundamental studies of beam dynamics in stellarator fields carried out under this contract are part of the necessary foundation for further experimentation and system design.

Prior to this experimental effort, it had been established that a single 180-degree stellarator bend magnet could transport a 1.4 kA, 900 keV beam without loss of charge (4.0 kG guide field, stellarator gradients up to 560 G/cm), and that the stellarator fields greatly increase the vertical field mismatch tolerance, especially for moderate guide field strength ( $\leq 10$  guide field Larmor periods per 360-degree toroidal revolution, as currently anticipated for near-term applications). However, in low guide field measurements (1.87 kG), loss

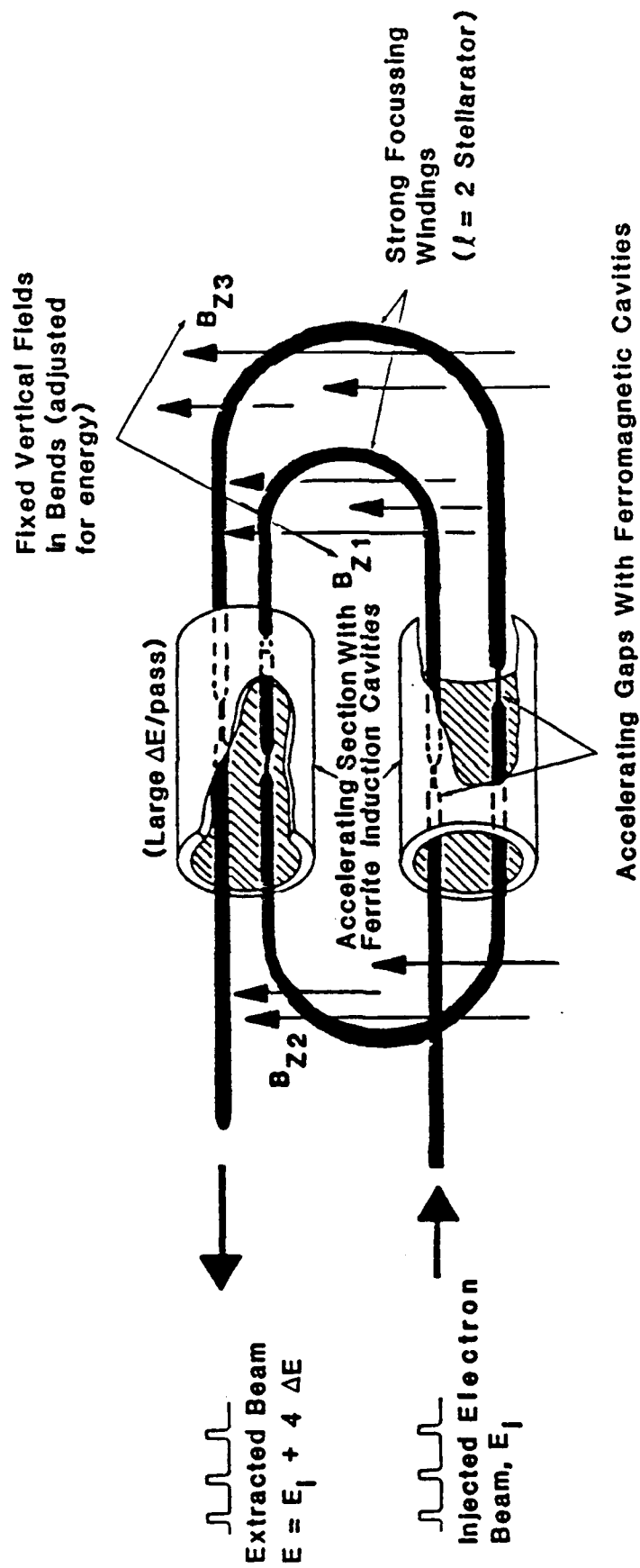


Figure 1. Conceptual layout of a 540-degree SLIA accelerator with two acceleration passes through each of two cavity arrays.

of the latter portions of the beam had been observed for high stellarator gradients through an unidentified mechanism. This observation, occurring in a parameter regime predicted by Hughes and Godfrey<sup>[4]</sup> to be unstable to a three-wave collective mechanism, required further investigation to determine the mechanism and means of its prevention.

The goals of this effort included quantitative comparison of theoretical and experimental beam centroid offsets as a function of vertical field mismatch and investigation of the beam tail loss phenomenon. Improved performance of the diode and compression region was also necessary to improve beam envelope matching and hence the resolution of time-integrated measurements of the emittance of the beam within the transport channel.

The beam offset for a beam current of 650 A and energy of 820 keV, with a guide field of  $\pm 3$  kG and stellarator gradients up to 600 G/cm, was found to agree to within  $\pm 3$  mm with the calculated offsets over the vertical field mismatch range of  $\pm 15\%$ . This provides experimental validation of the beam dynamics and centroid motion expected from theory. RF observations of the B-dot pickups in the beamline show strong excitation at a frequency slightly below 3 GHz, in agreement with the Hughes-Godfrey predictions. This excitation is present for sufficiently high stellarator gradient with electron Larmor rotation opposite in sense to the quadrupole rotation, and is absent with Larmor rotation in the same sense as the quadrupole rotation.

## 2.0 EXPERIMENTAL APPARATUS

The energy storage for the high voltage pulse power is a six-stage Marx bank, connected through a balanced charging circuit to a 5-ohm, 100 nsec water Blumlein line. This line is mismatched upward by a 5:3 impedance ratio into a 50 nsec coaxial water line, again through a 5:3 impedance step-up into a second 50 nsec water line, and finally through a vacuum insulator with a water resistor ( $\sim 40$ -ohms) in parallel with the  $\sim 650$ -ohm electron diode, for a final stage impedance step-up ratio of  $\sim 2.7:1$ . The net voltage step-up of  $\sim 2.3:1$  transforms the 500 kV maximum rated Blumlein output to over 1.1 MV. Along the



water line and Marx tank are several resistive and capacitive monitors to allow characterization of the pulse power. We have been using up to 400 kV output from the Blumlein, obtaining a pulse of up to 900 kV at the diode to enhance the shot lifetime of the velvet cathode.

The main pump for the diode vacuum chamber is a 10-inch cryopump, supplemented by two 50 l/sec turbopumps for backup and roughing use. The base chamber pressure is observed to be about  $1 \times 10^{-6}$  Torr. The transport line is directly pumped by the diode chamber. There is a pressure rise of approximately  $2 \times 10^{-5}$  Torr along its 2.8 meter length. The transport line consists of a straight tube of length 90 cm and inner diameter 3.48 cm (1.37 inch), and a 180-degree bend section of radius 0.5 meter (see Figure 2 for the overall layout). For the RF observations reported here, the Faraday cup was mounted in one of the older beamline sections, placed downstream from the bend exit. This allowed the introduction of a B-dot probe array between the bend exit and the Faraday cup. The straight pipe is surrounded by a two-layer solenoid winding (zero net axial current). The solenoid coil provides a stand-off between the compression region fields and the bend section fields. This stand-off also provides a region to check for emittance growth of the beam due to envelope mismatch and other transients before the beam enters the bend section magnet. The bend section incorporates straight extensions at either end of length 15 cm, and is of nominal inner diameter 6.02 cm (2.37 inch). The bend section magnets (Figure 3) include a twisted quadrupole winding of pitch length 18 cm and average radius 4.17 cm, surrounded by a two-layer solenoid coil, followed by a vertical field coil designed to provide a field index of approximately 1/2 over most of the magnet bore. The magnets are mounted on a wooden table to avoid magnetic interference from the support structure. The x-ray shielding in the experimental cell is of lead sheet of thickness 0.8 cm (5/16 inch) mounted on a plywood backing. The magnet power supplies are modular electrolytic capacitor banks<sup>[5]</sup> of 33.6 mF ( $24 \times 1400 \mu\text{F}$ ) capacitance, rated for 450 volts, and may be connected to charge in parallel and discharge in series.

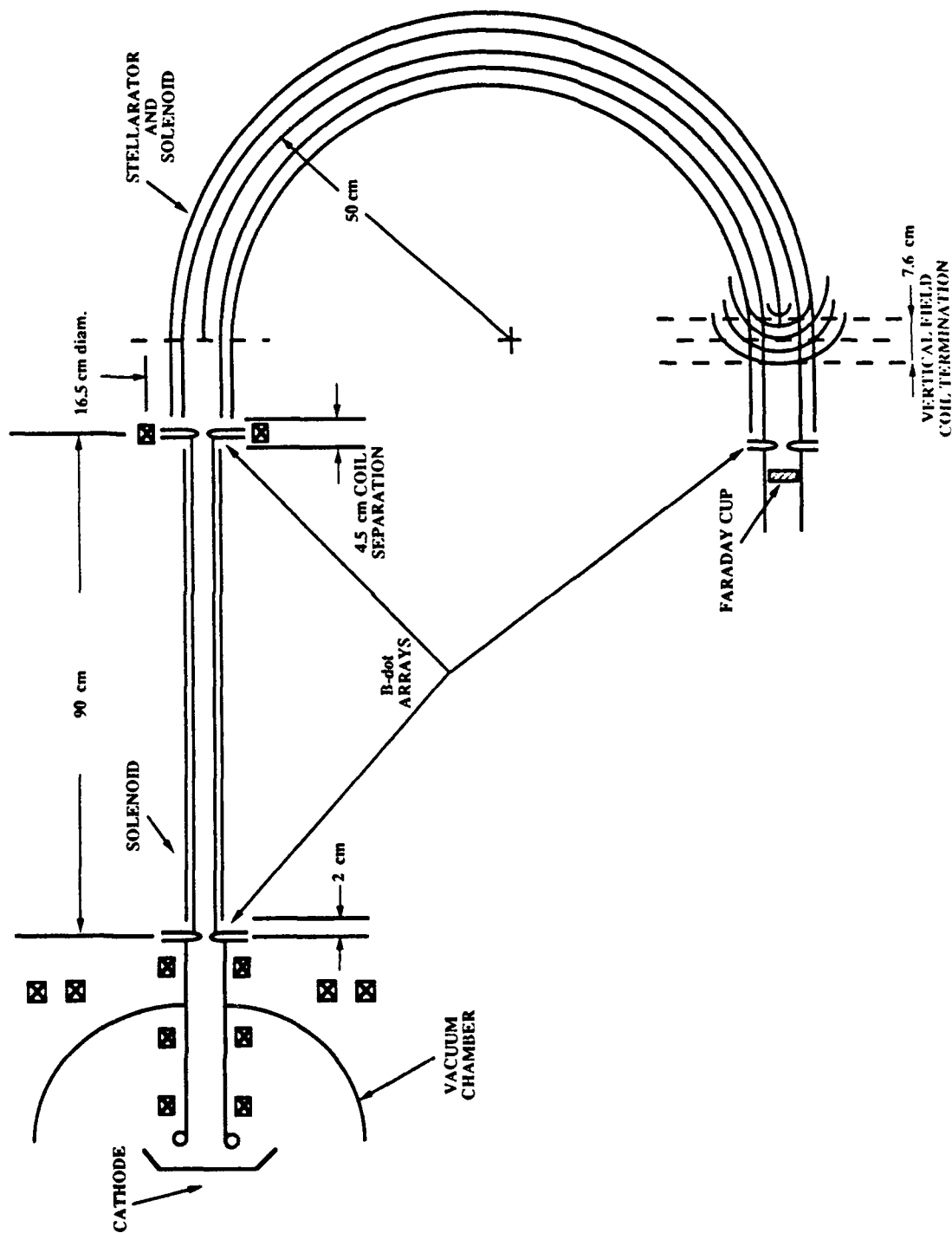


Figure 2. Schematic of the experimental setup. The diode chamber houses two vacuum coils mounted on the re-entrant anode. Two other coils are mounted on the exterior of the chamber. A Faraday cup can presently be mounted anywhere in the system except in the 90 cm solenoid. B-dot diagnostic arrays are currently mounted at the flange junctions from the injector to solenoid, solenoid to bend, and at the bend exit.

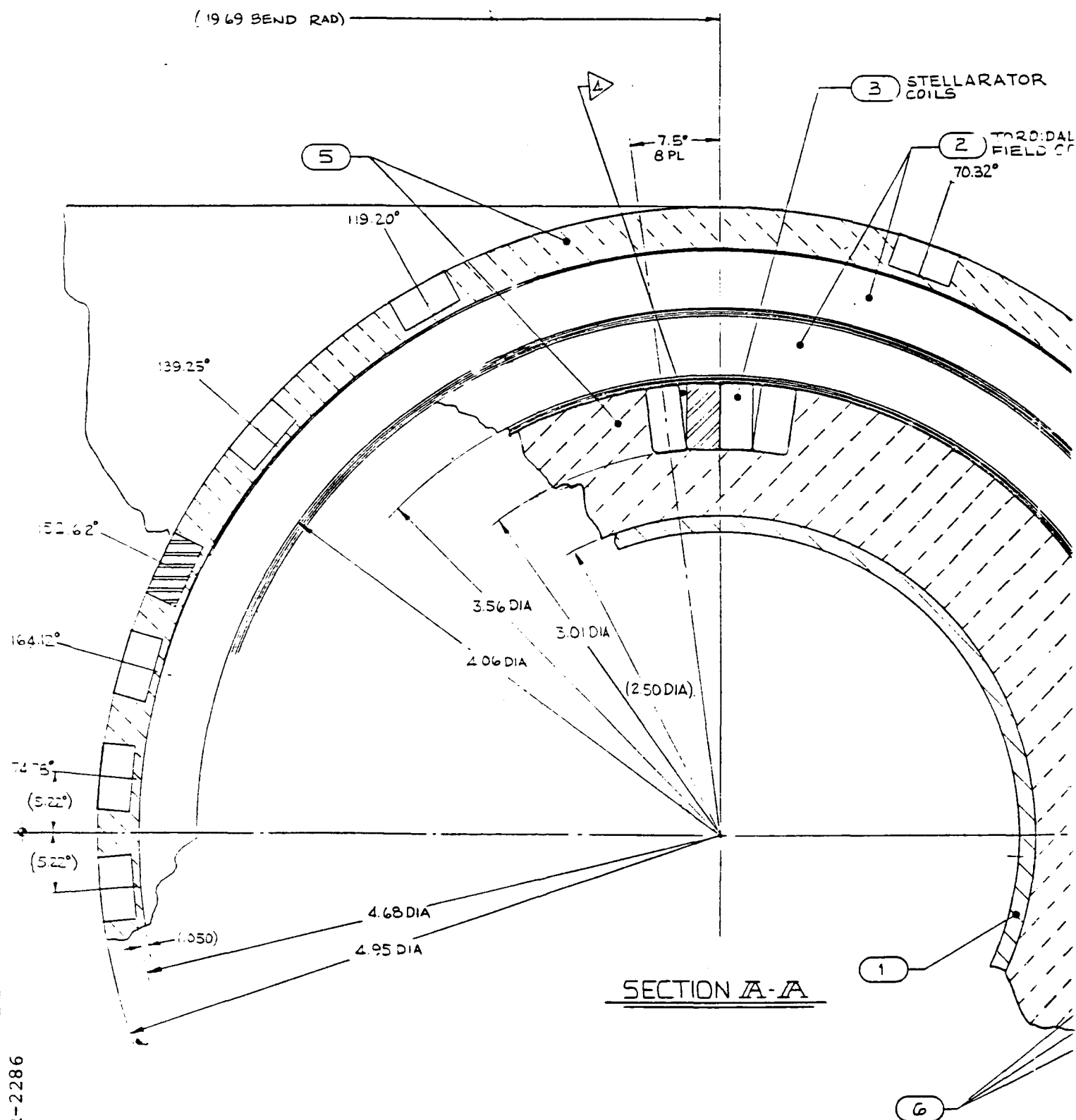


Figure 3. Engineering drawing of the cross-section of the bend magnet, showing the beam pipe and all magnet winding positions.

6-B

At each flange junction for the later experiments there was an assembly of four B-dot pickups, equally-spaced azimuthally, to enable monitoring the current and/or x-y position of the beam in time. Beam current was also measured by a totally absorbing Faraday cup, monitored by a stainless steel foil shunt (foil thickness 25.4 micron, overall resistance 72 m $\Omega$ ). This Faraday cup also served as a beam dump. There were also two capacitive monitors in the vacuum chamber for measurement of the diode voltage in the plane of the cathode field-shaper (Pierce electrode). The overall beam diameter and shape are determined by imaging the beam on a fused silica Cherenkov convertor. The convertor is also used to image the beamlets passing through a pinhole array plate in measurements of the emittance of the beam. The energy of the beam was low enough that the 0.9 mm titanium of which the pinhole plate is made is range-thick.

The data acquisition system consisted primarily of CAMAC digitizers, supplemented by oscilloscopes and gated and nongated film cameras. Phenomena occurring on the time scale of the beam (100 nsec) are recorded on one of four 5 nsec per sample digitizers, while slower data, such as the magnet bank currents, are recorded by one of 64 channels of digitizer capable of recording as fast as 25  $\mu$ s per sample. Eight channels of intermediate speed (as fast as 1  $\mu$ s per sample) are also used.

### 3.0 DIODE WORK

The original diode design by PSI, as modeled using EGUN (the Stanford Electron Trajectory Program) with no external magnetic field, is shown in Figure 4(a). Effecting radial compression of a large diameter, divergent beam over a short axial distance by means of external magnetic fields increases the sensitivity of the optics to chromatic variations. In order to minimize chromatic variation of the output beam, PSI designed a convergent diode to take advantage of the insensitivity of particle trajectories of nonrelativistic, space-charge-limited diodes to variation in the applied voltage. By accomplishing a large transverse compression within the diode, a smaller relative compression remains to be obtained from external magnetic fields. An EGUN calculation based on this design is

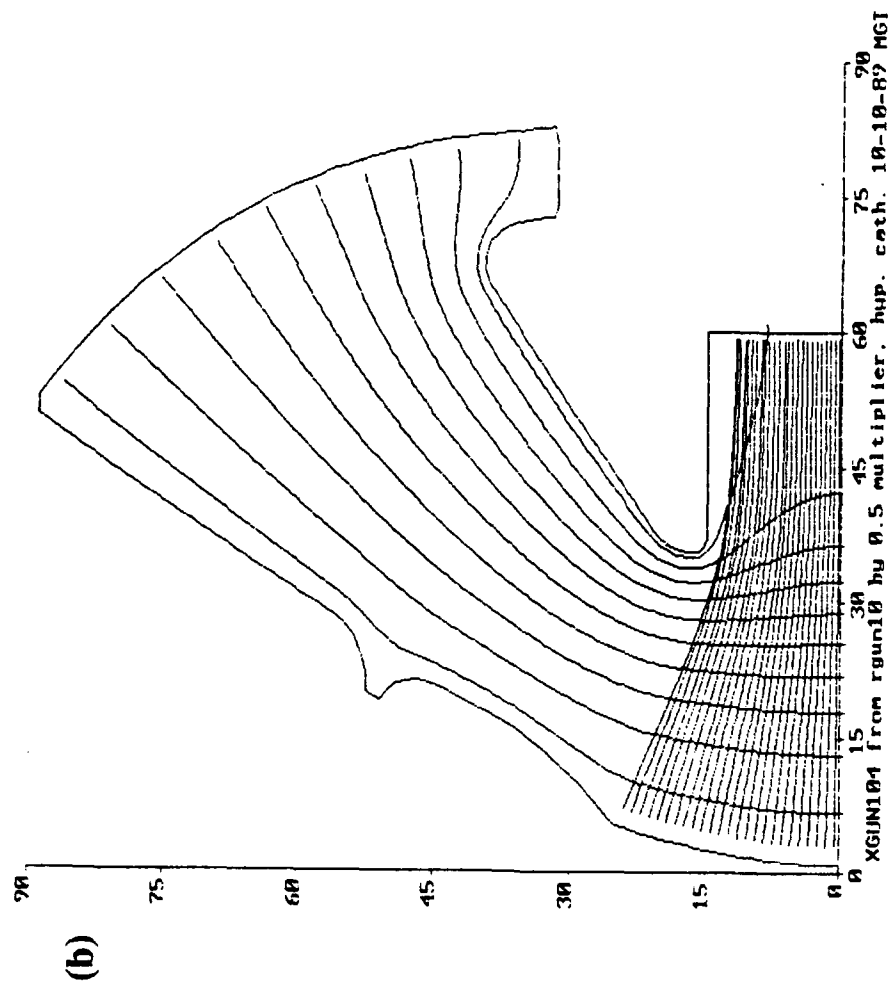
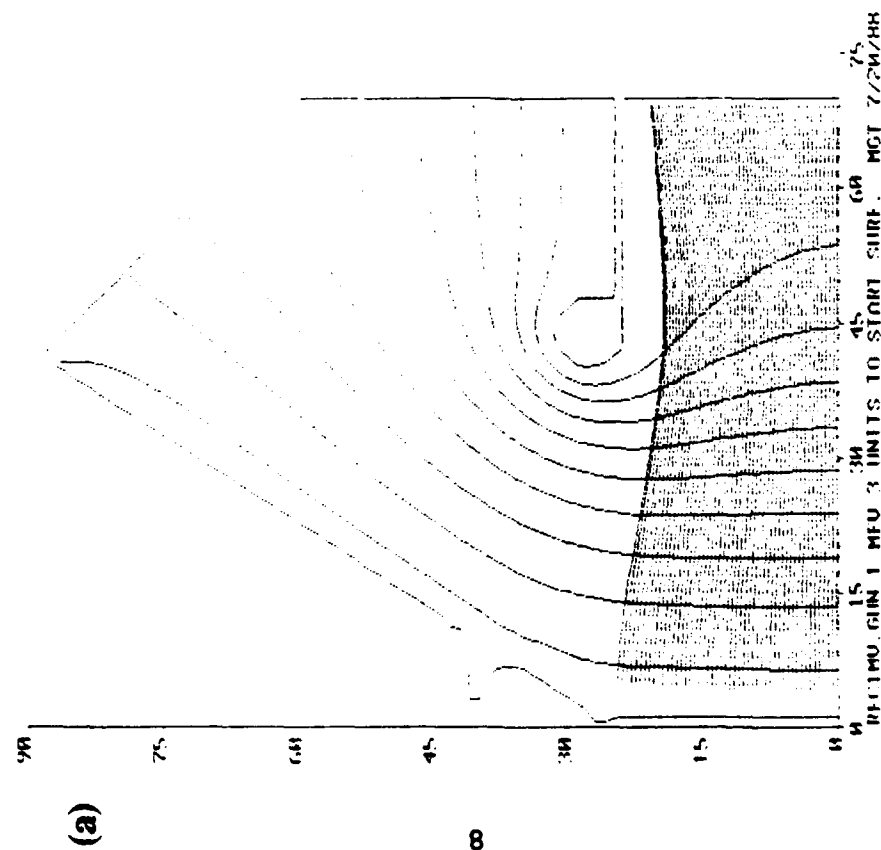


Figure 4. (a) Ray trajectories calculated with EGUN for the original experimental diode configuration. The beam enters the anode at a waist and then diverges, primarily under the influence of radial termination of the accelerating electric fields at the diode. (b) Ray trajectories from EGUN for a convergent geometry, resulting in a smaller beam in a smaller beam pipe, approximately at a waist after passing through the radial termination of the accelerating fields.

shown in Figure 4(b). This design exploits the fact noted by T. Hughes of Mission Research Corporation, Albuquerque that matching of a beam into a solenoid channel can be easier if the scale length of magnetic field variation is considerably shorter than the cyclotron period of the moving electrons. The small diameter anode tube allows use of smaller diameter field coils and hence reduces the scale length for changes in magnetic field. An added benefit is that the stray field variation at the cathode can be smaller than that for a larger diameter coil the same distance from the cathode. This diode has not yet been tested.

The compression region magnets were originally designed using steady-state magnetic fields, ignoring eddy current effects from the pulsed magnets, as a first approximation. This approximation is reasonable for the thin-walled beamline and connecting flanges, but fails to account for significant eddy currents in the diode chamber walls. To account properly for the magnetic field diffusion through the diode chamber, Hall probe measurements of the field were made at 1 cm intervals along the beamline axis at the time of peak current for each of the four discrete coils in or adjacent to the chamber. The axial field values were used in the envelope equation model of the beam compression region by scaling the measured fields proportionally to the coil currents and summing. When coupled with the flatter diode voltage pulse (improved under other funding to better than  $\pm 3\%$  over the center 65 nsec of the pulse), the improved beam envelope control enabled time-integrated emittance measurements with a resolution of approximately  $\pm 10 \pi$  cm mrad plus systematic uncertainties from aberrations of approximately  $\pm 20 \pi$  cm mrad.

Beam experiments and magnetic field measurements showed that the straight solenoid magnets fabricated earlier using tubing of the same size as that for the bend magnet had significant vacuum leaks and magnetic field errors. It was decided to use the existing diode, converging into a small-bore solenoid, for the remainder of the experiments. A straight solenoid was wound onto a 3.48 cm inner diameter stainless steel tube of overall length 90 cm. A second magnet was fabricated after nonuniformities in the first winding were noted visually and confirmed through magnetic measurements. Visible winding nonuniformities in the second magnet were avoided through improvements in the fabrica-

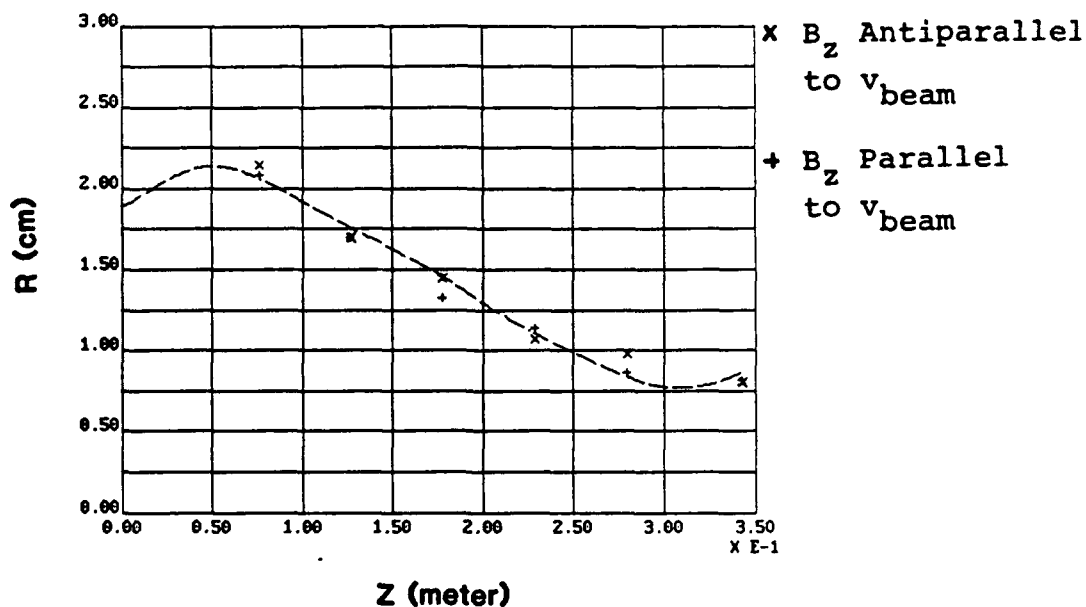
tion fixtures. Observed beam offsets at the end of the straight solenoid were  $\sim 5$ -7 mm for the original, large-diameter solenoid, 3-5 mm for the first small-diameter solenoid, and 1-2 mm for the second small solenoid, as determined from time-integrated imaging of the beam on a Cherenkov convertor.

The beam divergence after it enters the anode is typically large enough to require aperturing the beam to eliminate the outer portion; i.e. the part most subject to aberrations from the large aperture fields of the first focussing magnets. The aperture is placed at the mouth of the anode and it affects the beam optics by perturbing the electric fields at the transition from the diode region into the drift region inside the anode tube. Radius measurements of the beam at various locations in the anode tube are shown in Figure 5, for beam currents of 680 and 950 A. The envelope measurements are in very good agreement with envelope calculations (also shown in Figure 5) using the measured magnetic fields and beam emittances. The normalized emittance measured from pinhole array imaging, without correction for spherical aberration (or for non-zero magnetic field off-axis at the cathode) is approximately  $23 \pi$  cm mrad for the 650 A beam and  $73 \pi$  cm mrad for the 950 A beam. These measurements were made at different times and with different compression region fields. The corrected normalized emittances are approximately  $50 \pm 25 \pi$  cm mrad for the 680 A beam, the uncertainty due largely to spherical aberrations apparent in the data, and  $73 \pm 20 \pi$  cm mrad for the 950 A beam, the error being dominated by measurement uncertainty. These values are quoted for approximately twice the RMS half-width in both angular and spatial distributions.

Voltage and current waveforms for the diode are shown in Figure 6. The voltage trace is measured by an externally integrated D-dot probe. The current waveform is of slightly shorter duration than the voltage waveforms, indicating a turn-on delay of  $\sim 5$  nsec at the present applied field and  $dV/dt$  values. The diode has been operated at 1 MV, but the vacuum chamber voltage diagnostics tend to fail as a result of surface emission late in the main pulse. To reduce field emission from the cathode and minimize post-pulse damage to the velvet emitter surface, operation has been limited to 900 kV. The injector



(a)



(b)

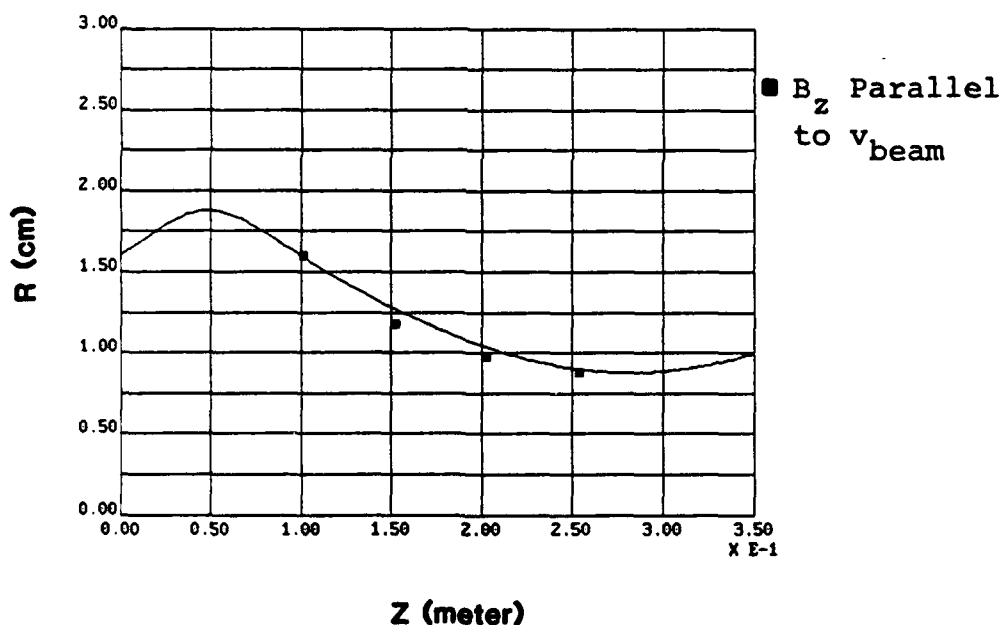


Figure 5. The measured envelope radius of the beam within the anode tube is shown, along with an envelope equation calculation (solid lines) using the measured applied fields, beam current, and beam emittance for (a) 950 A with an emittance of  $100 \pi$  cm mrad, with the initial conditions chosen to fit the measured envelope; and (b) 650 A with an emittance of  $50 \pi$  cm mrad, using the measured envelope radius and convergence angle at the point 10.2 cm downstream from the anode entrance.

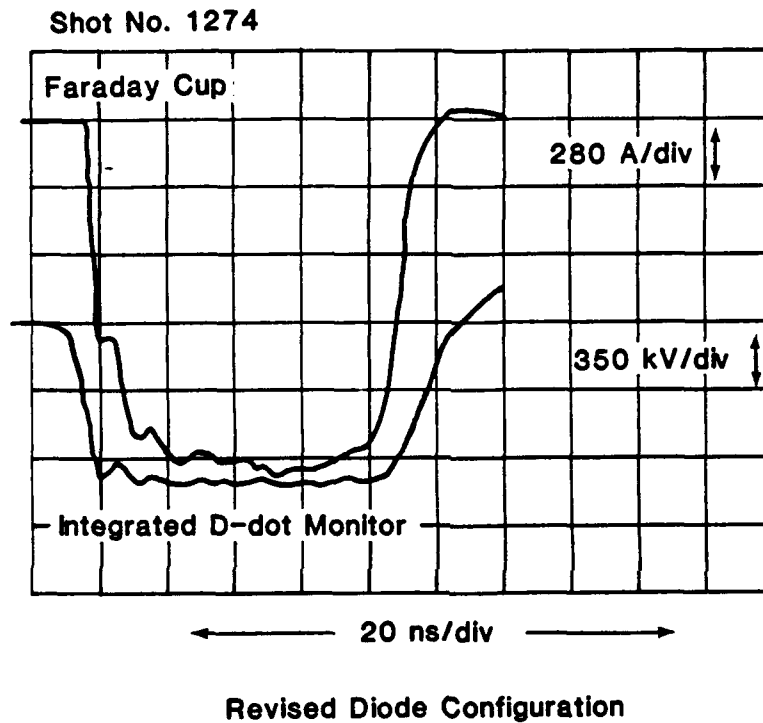


Figure 6. The measured diode voltage and current for operation at approximately 900 keV, without aperturing of the beam. The voltage trace shown is from a passively integrated D-dot probe (a piece of 6.4 mm diameter semi-rigid coaxial cable cut off flush with the interior of the vacuum chamber in the plane of the cathode field shaper). The current trace is from the Faraday cup mounted in the anode pipe.

now performs well and is capable of supplying up to 1.4 kA (unapertured) for the 80 nsec central portion of the pulse.

#### 4.0 MAGNET MAPPING

The large-bore straight magnet made under prior funding has been shown under another contract to have localized transverse perturbations at the level of approximately 5% of the axial magnetic field. These perturbations explain earlier observations of beam offsets at the exit of the straight magnet, and were part of the reason for fabricating a new 90 cm solenoid. One major purpose of the straight magnet is to maintain the spatial separation of the injector and compression magnets from the bending magnet. The first new magnet was wound on a stainless steel tube 90 cm long (including flanges), of outer diameter 3.8 cm (1.5-inches) and wall thickness 0.17 cm (0.065 inches), using round magnet wire of 0.27 cm diameter (#8 AWG). The windings of the first magnet were not azimuthally symmetric (the axial component of the current was unevenly distributed around the pipe). The effect of winding asymmetries can be estimated from an ideal solenoid with  $N$  turns per meter, carrying a current of  $I$  amperes, superimposed with an equal axial current  $I$  distributed uniformly over half of the azimuth of the solenoid, at the winding radius  $R$ . Such a magnet has a net field in the central region of the magnet with a fractional component perpendicular to the solenoid axis of

$$B_{\perp} / B_z = \frac{1}{N \pi^2 R}$$

For the 2.05 cm radius of the inner layer of the new solenoid, with no space between the windings, the fractional error is approximately 1%. This estimate is consistent with measurements made under other funding on this magnet, in which transverse fields on-axis of  $\sim 1/2\%$  of the guide field were noted.

A second magnet was fabricated with the addition of tapered spacers at the ends of each winding layer to set the desired pitch from the beginning, and the addition of a layer of 0.25 mm stainless steel shim stock between the layers to prevent the second layer from conforming to the (opposite helicity) inner layer, as observed on the first magnet. The insulation of each layer of magnet wire was protected from the shim stock edges by a layer of Kapton tape. The uniformity of windings on this magnet was excellent to visual inspection. The magnet was put into service without additional magnetic measurements, and the beam offset at the exit of the solenoid immediately dropped to 1-2 mm from 3-5 mm for the first small-bore magnet.

## 5.0 EMITTANCE

Greater stability in the applied voltage and an improved magnetic compression region have enabled meaningful time-integrated emittance measurements. The values of emittance at the injector, along with those at the exits of the straight solenoid and bend sections, both corrected and uncorrected for aberrations, are given in Table 1. The data indicate that emittance growth may be quite small in stellarator fields, but the cumulative effect of many focussing transitions is still uncertain. The guide field was -3.0 kG, with a peak beam current of 680 A and a stellarator gradient of 400 G/cm. (The guide field was anti-parallel to the direction of propagation of the beam.)

Table 1. Normalized beam emittances ( $\pi$  cm mrad).

<u>Axial Location</u>	<u>Uncorrected</u>	<u>Corrected</u>
Injector Exit	23	$50 \pm 25$
Solenoid Exit	32	$50 \pm 25$
Bend Exit	30	$50 \pm 25$

## 6.0 DISPERSION

Dispersive effects in the existing beamline were simulated by mismatching the vertical field to the particle momentum and measuring the resulting beam offset at the exit of the bend. The diode voltage was measured with a capacitive monitor about 40 cm upstream from the diode. The beam current (680-700 A peak) was measured with a resistively monitored Faraday cup and monitored for shot-to-shot uniformity with B-dot probes mounted between beam pipe segments. A fused silica Cherenkov convertor imaged the beam for envelope measurements and imaged the beamlets from a pinhole array for emittance measurements. We used a polaroid film camera for time-integrated measurements.

The beam is centered to within approximately 1 mm within the injector and at the end of the straight solenoid. The beam centroid at the end of the 180-degree curved part of the bend section is offset toward the major axis by approximately 1.5 mm for a bending field of 92 G (chosen for vertical centering). Without beam space-charge and self-current corrections, the matched bending field is calculated to be 88 G.

Mismatching the vertical field results in a vertical drift of the beam as it transits the bend in the absence of stellarator focussing, resulting in beam spilling off the Faraday cup. The gross effect of stellarator focussing on the centering of the beam may be seen in Figures 7 and 8, showing the current at the exit of the bend intercepted on a Faraday cup of diameter 5.1 cm in the 6.02 cm diameter pipe, as a function of the vertical field strength for various stellarator gradients. The data of Figure 7 were taken at an energy of 850 keV, a guide field of 1.87 kG, and a beam current of 600 A, for stellarator gradients of 0 and 327 G/cm, and a beam current of 300 A for 562 G/cm. As the beam moves off-center and spills off the Faraday cup, the indicated current on the cup decreases. A gradient of 327 G/cm significantly broadens the response, showing that the beam is focussed toward the beam pipe axis by the quadrupole field. When the gradient was raised to 562 G/cm, the last 40 ns of the 100 nsec beam pulse was gradually lost. By reducing the size of the aperture at the anode to decrease the current injected into the channel to 300 A, the full beam pulse width

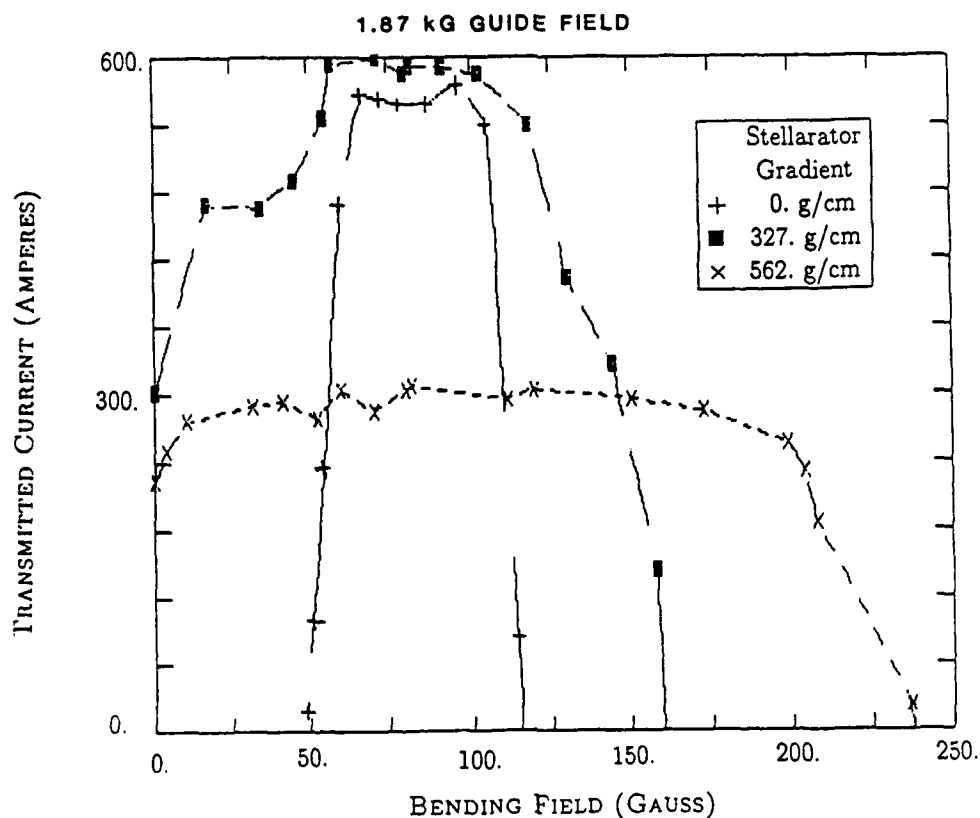


Figure 7. Effect of stellarator fields on beam transmission (stellarator focussing prevents beam from scraping the wall).

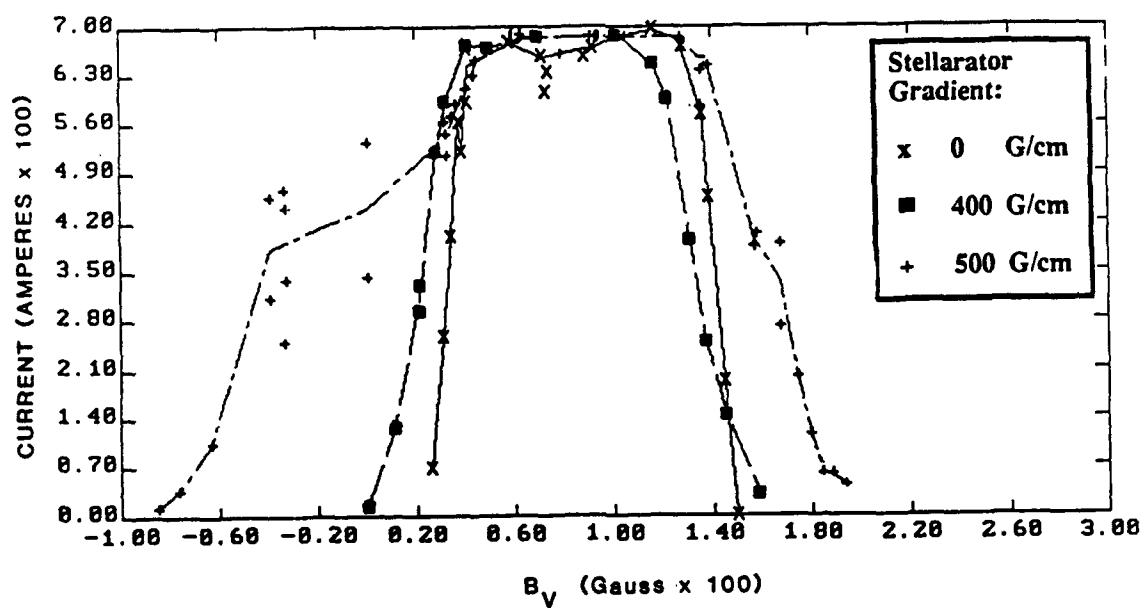


Figure 8. 900 keV, 700 A beam transport through bend with 3 kG guide field for varying bending fields. Stellarator effect becomes noticeable at 500 G/cm when viewing current passband at this guide field level and particle energy.

was again passed. The beam loss phenomenon is discussed below. The current transmission through the stellarator bend for the 900 keV, 680 A beam at a guide field strength of 3 kG is shown in Figure 8. The shape of the curves is similar to those of Figure 7, but the effect of the stellarator field, as expected from calculation, is not as pronounced as it was for the 1.87 kG example. [The centroid drift with the guide field and vertical field alone is small for a 900 keV beam at 3 kG guide field.]

Figures 9(a) through 9(d) show centroid offset measurements and calculated values for a guide field of 3 kG and stellarator gradients of 300, 400, 500, and 600 G/cm, using 825 keV for the electron kinetic energy. The zero current matched vertical field at this kinetic energy is 82 G. The offset was measured from open-shutter photographs of a Cherenkov converter/crosshair assembly inserted into the beamline. The displacements were calculated using a first-order formalism for the centroid, including wall image forces. The calculations assume linear focussing forces and are valid for small displacements of the beam centroid from the axis of the bend and are not accurate very far beyond approximately  $\pm 15\%$  equivalent energy variation (corresponding to vertical field extremes of 72 and 92 G). The reference energy for each value of the vertical field strength is the energy matched to that field. The beam energy is treated as perturbed from the kinetic energy of a matched beam.

The beam offset with vertical field mismatch is in the vertical direction for zero stellarator gradient. The offset has been rotated into the horizontal plane (the plane of the bend) by the stellarator field at a gradient of 300 G/cm, as shown in Figure 9(a). The horizontal motion increases as the gradient is increased to 400 G/cm (Figure 9(b)), rolling off through 500 G/cm (Figure 9(c)) and 600 G/cm (Figure 9(d)). The vertical motion is eliminated near the matched field of 82 G for a gradient of 500 G/cm, reversing sign for 600 G/cm. The agreement of calculation with experiment is very good, especially over the span of  $\pm 15\%$  about the matched energy.

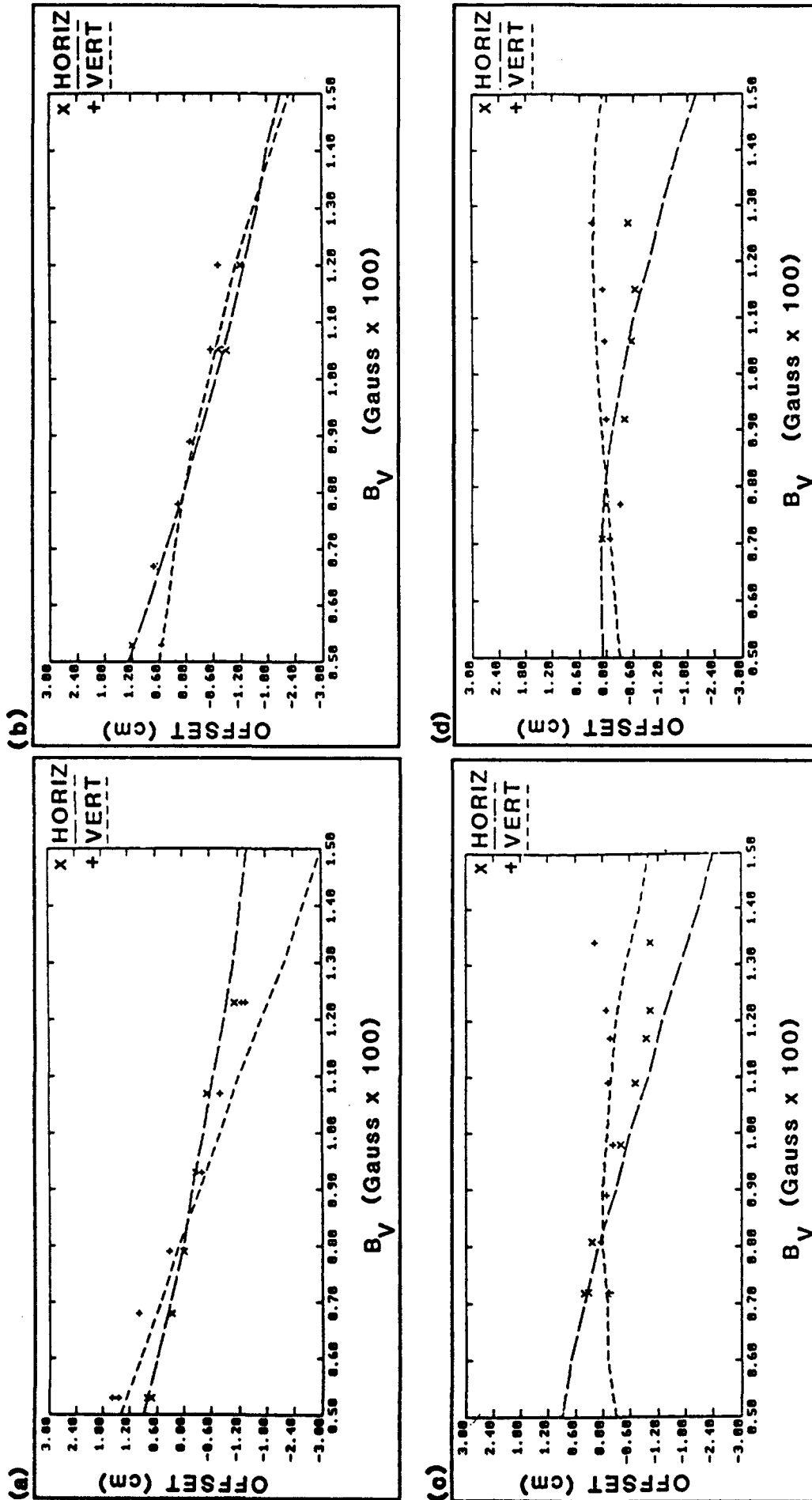


Figure 9. Experimental beam centroid offsets vs. calculations from first-order expansion (3 kG guide field parallel to electron directed velocity). (a) Gradient of 300 G/cm has converted much of vertical drift without stellarator field into horizontal motion, though vertical motion dominates the offsets; (b) 400 G/cm gradient, horizontal and vertical offsets are approximately equal; (c) 500 G/cm, vertical offset nearly constant, horizontal offset nearly identical to (b); and (d) 600 G/cm, vertical offset beginning to change sign, while horizontal offset is rolling off.



For the 18 cm winding period of the bend section stellarator coil, a guide field of 3 kG results in a dynamical reduction of the average focussing of the beam centroid because one of the oscillation frequencies becomes very low. Reversing the guide field shifts this frequency to higher values, and restores the overall focussing. The comparison is shown in Figures 10(a) through 10(c). The beam at the bend exit in this reversed configuration is well centered over an extremely wide range of vertical field mismatch for a gradient of 300 G/cm. [At 300 G/cm, the calculational values are valid only up to  $\sim 130$  G.] Within the bend section the calculated excursion is on the order of 1 cm, however. The agreement with the first-order calculation is again excellent for the 200 and 300 G/cm gradients over the  $\pm 15\%$  energy range.

## 7.0 COLLECTIVE PHENOMENA

In the course of work prior to this program, an unexplained loss of beam was observed in the later portions of the beam pulse when the guide field was oriented parallel to the direction of electron motion. These experiments were carried out at a guide field of 1.87 kG with a beam current of 600 A and an energy of 850 keV. As the stellarator gradient was raised above 400 G/cm, an erosion of the tail of the beam began, affecting approximately the final 30-50 nsec of the 100 nsec pulse at a gradient of 560 G/cm. The B-dot probes near the bend entrance showed evidence of breakdown (discharge) near the end of the beam pulse, and for a time locally high gas pressure resulting from known small leaks in the B-dot assembly was suspected as the cause of beam loss. No beam loss occurred when the injected beam was apertured to half of its former current. Later work under other funding established that as much as 1400 A could be transported without loss at a stellarator gradient of 560 G/cm and a guide field strength of 4.0 kG, and that the 1.87 kG loss was unaffected by lowering the transport line background pressure by an order of magnitude to  $\sim 2 \times 10^{-5}$  Torr.

These observations argue for a collective loss mechanism related to the stellarator gradient. There was a prediction made in 1985 by Hughes and Godfrey<sup>[4]</sup> that a three-

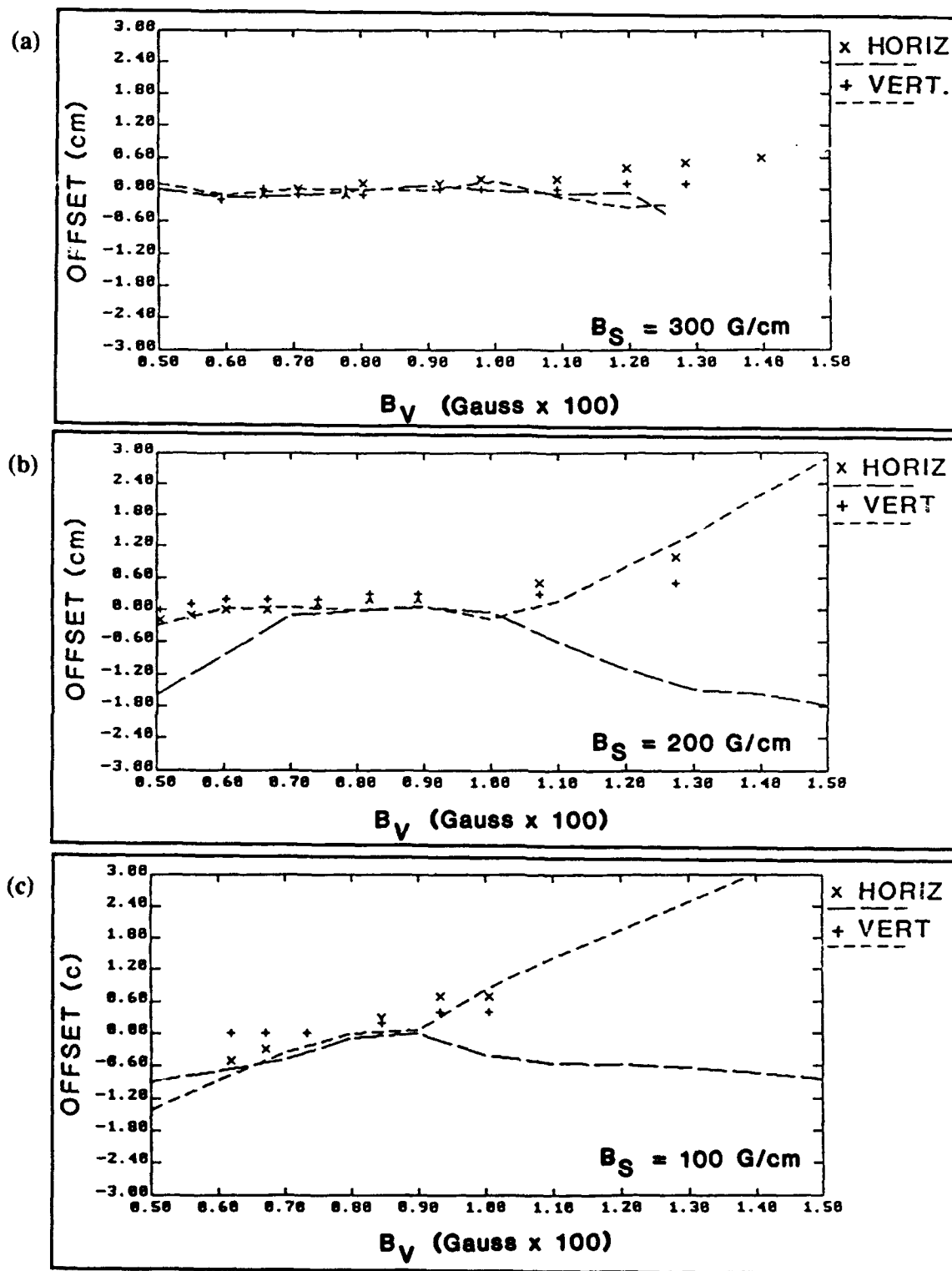


Figure 10. Guide field of 3 kG anti-parallel to electron directed velocity. [Note that both horizontal and vertical offsets are very small and nearly constant with a 300 G/cm stellarator gradient (a).] The Larmor rotation of the electrons is in the same sense as the quadrupole field rotation, with very nearly the same rate for these parameters.

wave resonance mechanism might be operative in the focussing regime of the experiment. Under present funding, radio-frequency power detectors, filters, and attenuators were obtained to permit measurement and analysis of any high-frequency signals on the B-dot probes.

The present experiments were carried out at the slightly higher energy of 900 keV with currents of 325, 680, and 950 A, guide field strengths of 1.2, 1.8, 2.4, and 3.0 kG, and stellarator gradients ranging up to 600 G/cm. Faraday cup beam current measurements confirm the tail erosion observed earlier (see below). RF measurements show strong excitation of the beam and of a waveguide mode coupling to the B-dot probes with a frequency very close to the 2.92 GHz cutoff frequency of the TE<sub>11</sub> mode in the beamline, in agreement with the predicted frequency. Diagnostic RF filters used were low-pass filters with measured -6 dB points of 2.89, 3.14, and 4.23 GHz, and a high-pass filter with a -6 dB point of 2.77 GHz. The RF detectors used were HP 8471E planar doped barrier diode detectors specified for the frequency range 0.01-12 GHz. Characteristics of attenuators and power tees and were checked for frequencies up to 6 GHz with a Hewlett-Packard 8753C network analyzer and 85047A S-parameter test set prior to use.

## 8.0 RF PICKUP

The B-dot pickups are electrostatically shielded from the beam by mounting them in an annular housing designed to fit between vacuum flanges of the beamline. There is an azimuthal slot in the housing to allow penetration of the azimuthal magnetic field they were designed to sense, the magnetic field of the beam. The structure around the B-dot probes affects their pickup characteristics as a function of frequency, in addition to variations due to stray capacitance and self-inductance. The overall sensitivity is shown in Figure 11, a frequency sweep of the B-dot response made with a network analyzer with the B-dot array mounted in a 50-ohm coaxial fixture. The B-dot probe outputs are essentially identical within a given array. The response is linear in frequency to beyond 1 GHz, except for small periodic variations (including one at multiples of about 165 MHz, corresponding to the

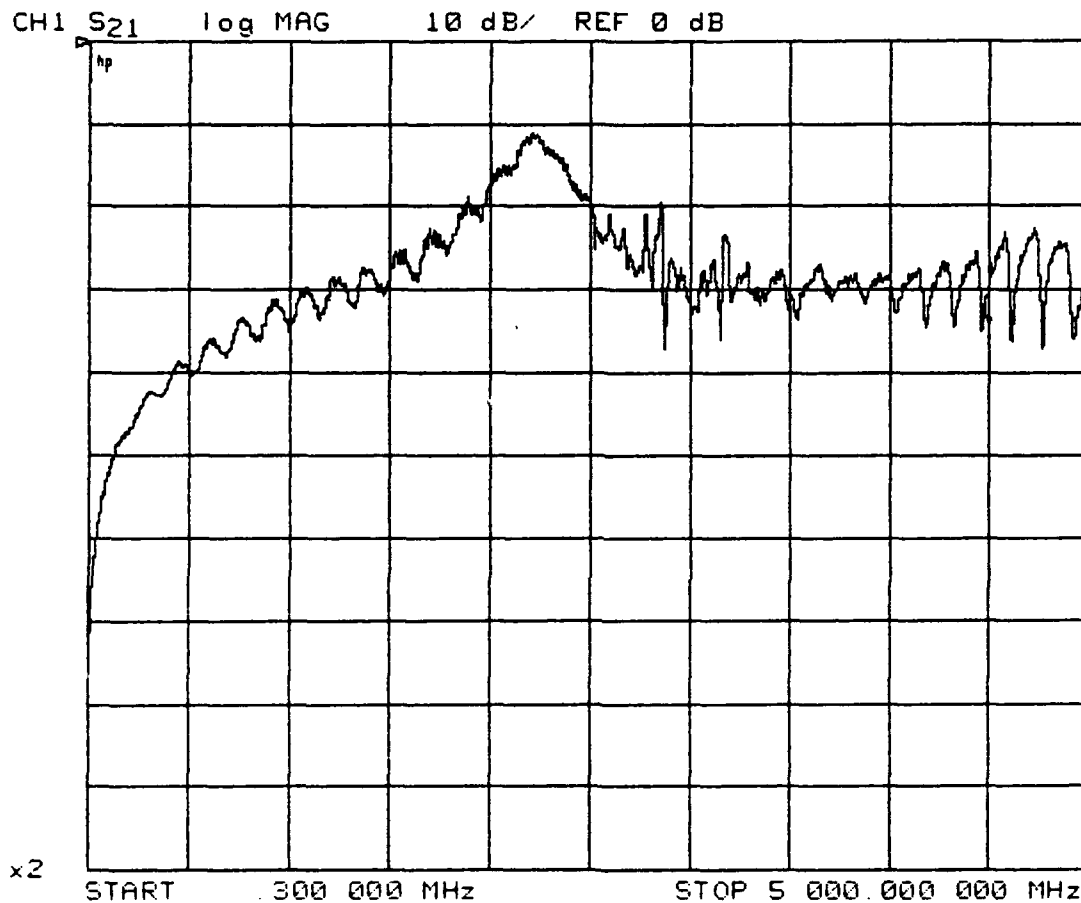
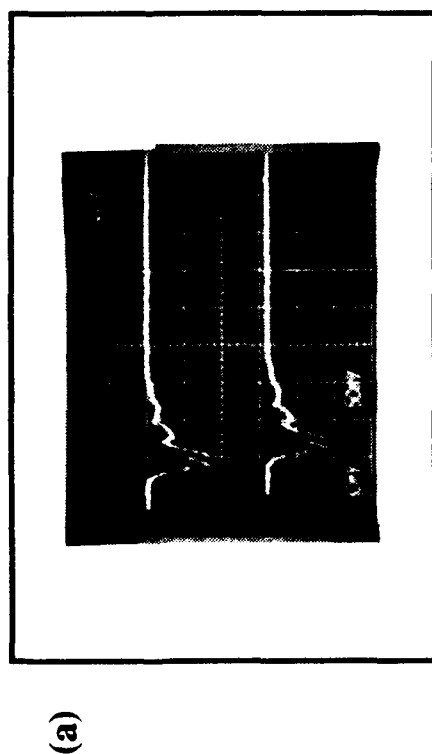


Figure 11. A network analyzer frequency scan of the B-dot array response, when mounted in a 50-ohm coaxial fixture. The standing wave frequencies (at multiples of approximately 165 MHz) are visible, and are the primary source of structure in the response curve below 1.5 GHz. The other resonance frequencies are not yet firmly identified.

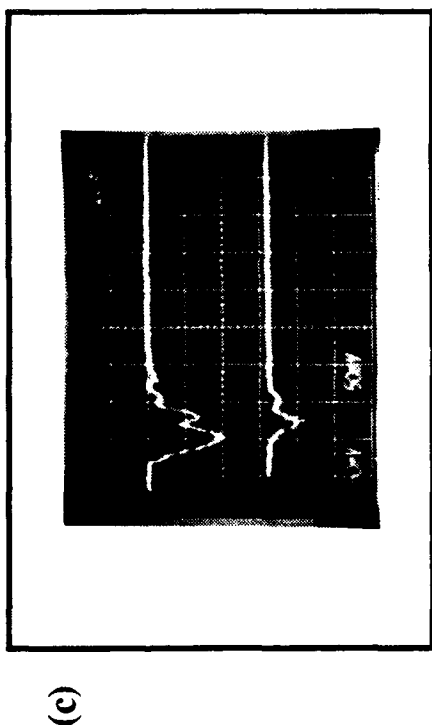
TEM standing wave excitations of the measurement fixture). There are significant variations above 1.5 GHz.

Most of the RF observations were made with a beam current of 950 A, a guide field strength of 2.4 kG, and a stellarator gradient near 250 G/cm, below the onset of beam loss at about 400 G/cm for this current and guide field strength. The first set of measurements was made using a 325 A beam in a 1.2 kG guide field with a stellarator gradient of 400 G/cm, shown in Figure 12. The output from a single exit B-dot was split through a Tee and fed into two HP-8471E diode detectors. The unfiltered outputs of Figure 12(a) are identical, and when a 2.77 GHz high-pass filter is put into the signal path for the upper trace and a 3.14 GHz low-pass filter is put into the signal path for the lower trace of Figure 12(b), the signals remain closely equal in magnitude. The frequency of the RF is thus between the 2.77 and 3.14 GHz rolloff frequencies of these two filters. In Figure 12(c), the upper trace has a 4.23 GHz low-pass filter in series, and the lower trace has a 2.89 GHz low-pass filter. The upper trace amplitude is almost exactly that passed by the two filters of Figure 12(b), but the trace with the 2.89 GHz low-pass filter passes only about 40% of the power of the other filter. Thus the frequency should be very close to, and slightly below, 2.89 GHz. The only mode able to propagate near this frequency in the 6.02 cm inner diameter (nominal for the tubing prior to bending) circular beam pipe is the TE<sub>11</sub> mode, with a 2.92 GHz cutoff frequency. In Figure 12(d) the temporal evolution of the RF signal may be seen, synchronized with the integrated signal from the same B-dot. Subsequent time domain measurements under other funding, using a 6 GHz Tektroniz 7250 single-shot scan conversion digitizer, indicated that the signal is a very pure sine wave of frequency 2.90 GHz ( $\pm 2\%$ ).

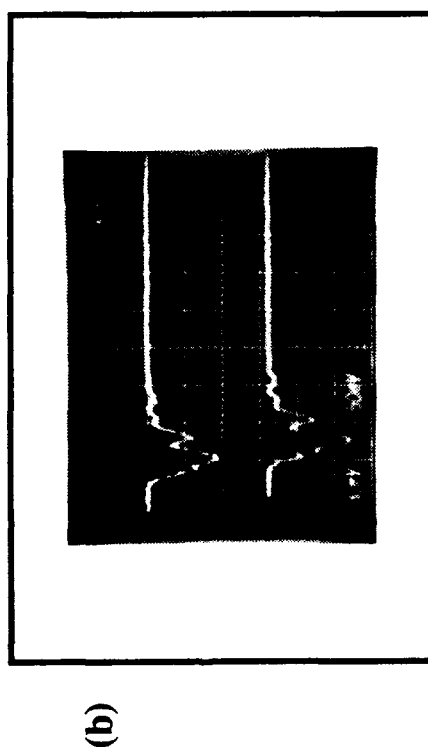
The remainder of the RF data were taken with a beam current of 950 A, a guide field strength of 2.4 kG, and various stellarator gradients. Figure 13(a) shows the output of the diode detector (risetime of 2-3 nsec into 50-ohms) for zero stellarator gradient with 36 dB of attenuation and no filtering between the B-dot (at the bend entrance) and the detector. The large-amplitude transients at the head and tail of the beam are clearly visible, and the coupled RF power is approximately 10 W. In Figure 13(b), the bend exit beam pickup



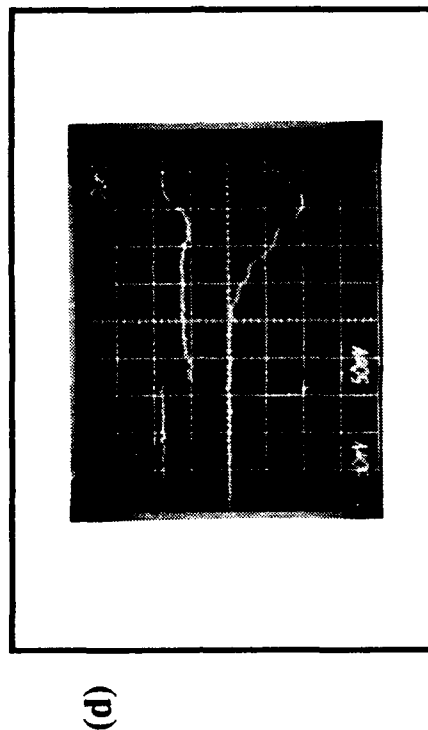
100 ns/div, 480 W/div



100 ns/div, 480 W/div



100 ns/div, 480 W/div



20 ns/div, 480 W/div

Figure 12. Exit B-dot branched through a "Tee" to two diode detectors for 325 A at a guide field strength of 1.2 kG. (a) Both traces unfiltered; (b) upper trace: 2.77 GHz high-pass, lower trace: 2.89 GHz low-pass filters, and (c) upper trace: 4.23 GHz low-pass, lower trace: 2.89 GHz low-pass filters. The two filters in (b) pass essentially the same power as in the unfiltered case. The 4.23 GHz low-pass filter in (c) passes the same power again, while the 2.89 GHz low-pass filter passes only 40% of the unfiltered power. The peak RF signal occurs at the end of the beam pulse as shown in (d), the slow integral of the B-dot (upper trace, arbitrary scale) and the RF detector output are shown in synchronization at 20 ns/div.

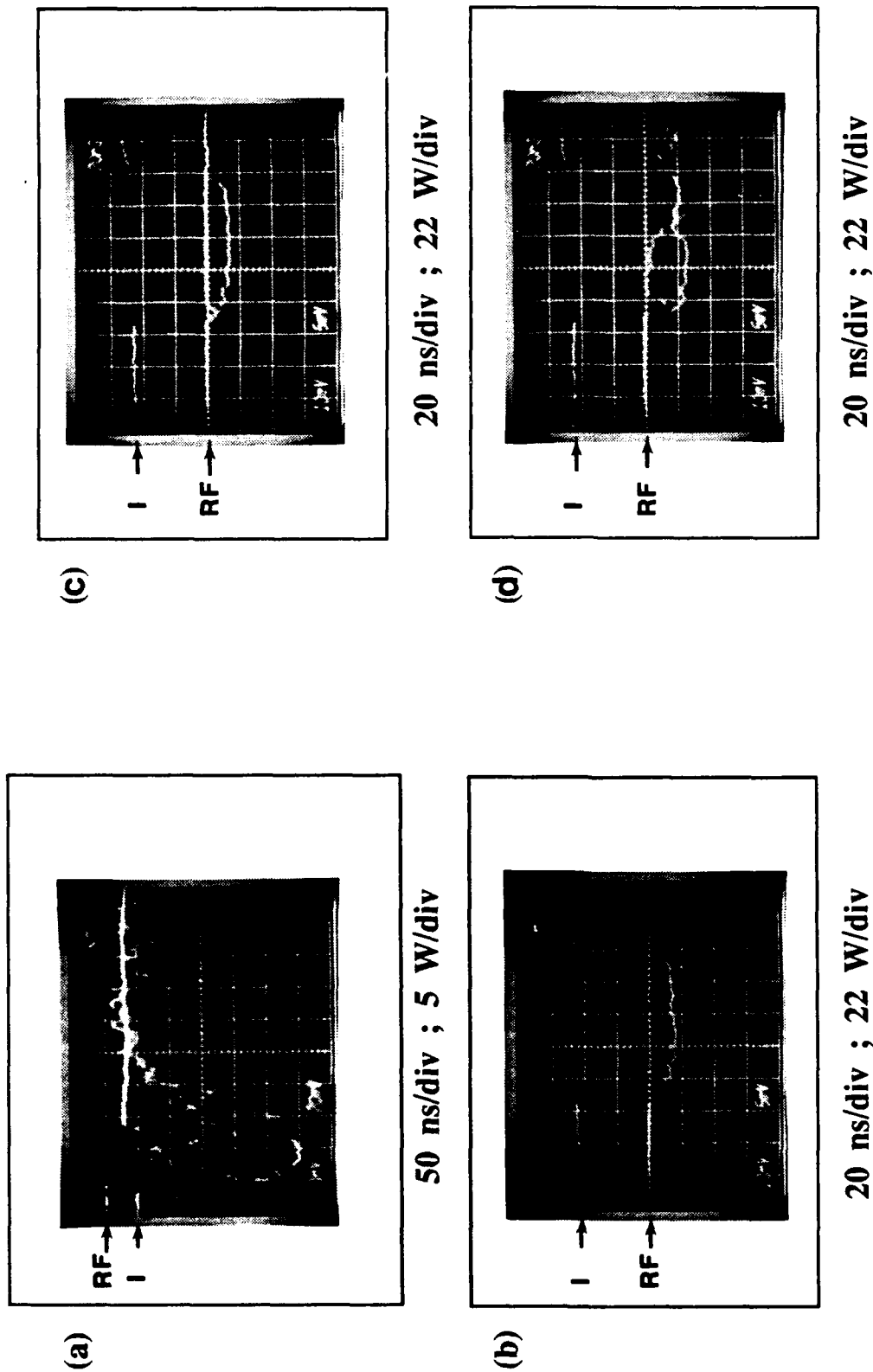


Figure 13. Diode detector output from B-dot probes. (a) Unfiltered at bend entrance with stellarator gradient 0 G/cm, RF attenuation 36 dB; (b) unfiltered at bend exit with stellarator gradient 100 G/cm, RF attenuation 50 dB; (c) 2.78 - 3.15 GHz bandpass filter at bend exit with stellarator gradient 100 G/cm, RF attenuation 50 dB; and (d) filtered bend exit with stellarator gradient 200 G/cm, RF attenuation 56 dB. The beam current is 950 A and the guide field strength is 2.4 kG for these measurements. The attenuation values given are exclusive of cable and connector losses.

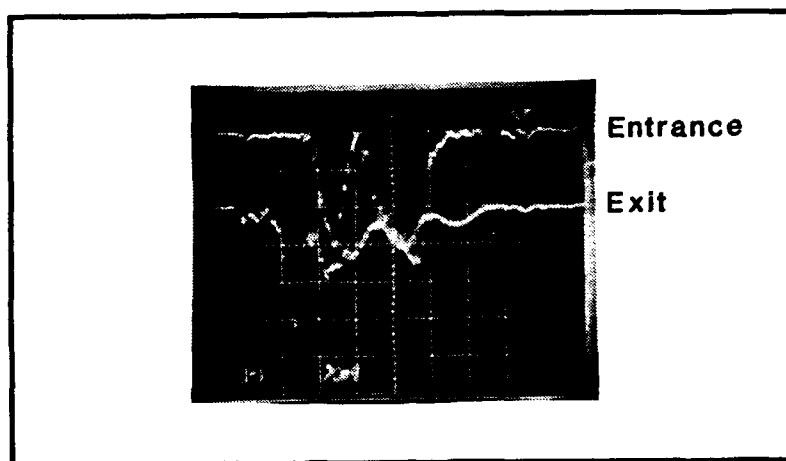
is shown with 50 dB of attenuation, without filters, and with a stellarator gradient of 100 G/cm. The steady-state pickup power during the beam pulse is about 30 W. The effect of adding 2.78 GHz high-pass and 3.14 GHz low-pass RF filters is seen in Figure 13(c), where the narrow-band signal near 3 GHz for the conditions of Figure 13(b) is seen to be at a level less than 1 W. Upon raising the stellarator gradient to 200 G/cm in Figure 13(d), the signal through the 3 GHz filters is clearly visible. With the 50 dB of attenuation in place, the power level corresponding to the on-screen threshold is approximately 90 W. Unfiltered signals from both the entrance and exit B-dots are shown in Figure 14, with 56 dB of attenuation on each channel. The beam current is 950 A, with a guide field strength of 2.4 kG and a stellarator gradient of 250 G/cm. No significant RF power is detected at the entrance B-dot until after the beam passes by the probe entirely. The peak power at both entrance and exit B-dot probes is approximately 2000 W. The power detected at the entrance of the bend is apparently associated with a waveguide mode propagating slowly in the beamline. If the first pulse seen at the entrance B-dot is a reflection of the power at the exit B-dot (the major-radius separation of the B-dot assemblies is 188 cm) then the group velocity corresponding to the  $\sim 40$  nsec temporal separation in peak power is  $\sim 0.16$  c. Because the group velocity  $v_g$ , cutoff frequency  $\omega_c$ , and frequency  $\omega$  of the mode are related through

$$\frac{v_g}{c} = \sqrt{1 - \left(\frac{\omega_c}{\omega}\right)^2}$$

the frequency must then be within about 1.5% of the cutoff frequency of the mode. This is consistent with the frequency determinations listed above.

The temporal growth of signals at the exit B-dot is shown in Figure 15 for various beam and focussing parameters. In Figure 15(a), the beam current is 325 A, the guide field strength is 1.2 kG, and the stellarator gradient is 400 G/cm. The growth of the signal is approximately exponential with a (power) growth time of approximately 18 nsec, half the growth time of the mode field and beam offset. The rise is uneven, punctuated with a plateau in power every 15-20 nsec. This same feature of the RF power versus time is seen in most of the data, and adds to the uncertainty in the measurement of the growth rate. For a

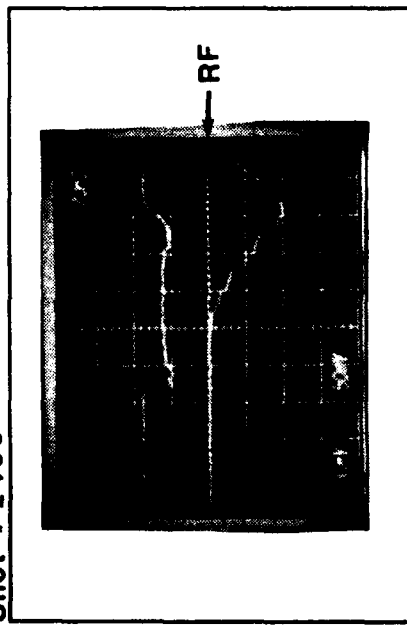




20 ns/div ; 630 W/div

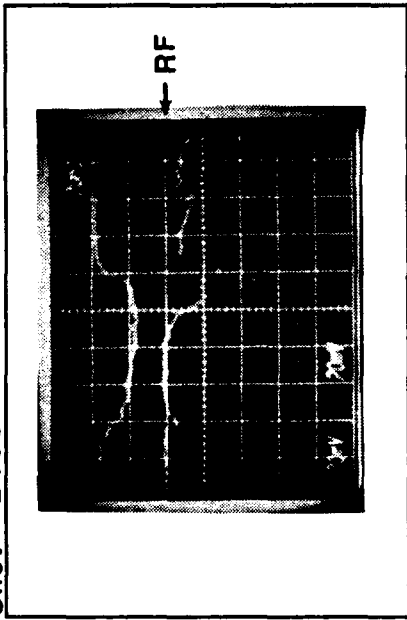
Figure 14. B-dot probe signals at the entrance (upper trace) and exit (lower trace) of the bend magnet from the same shot processed through two HP 8471E diode detectors. Peak power coupled out through each B-dot probe is  $\sim 2000$  W. The delay between the first peaks of the signal at the two locations is  $\sim 40$  ns, corresponding to a velocity of propagation of about  $0.16 c$  over the 188 cm spacing between the probes.

Shot #2405



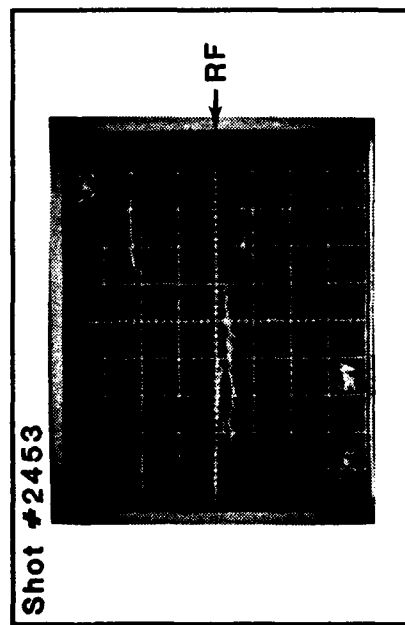
20 ns/div ; 480 W/div

Shot #2465



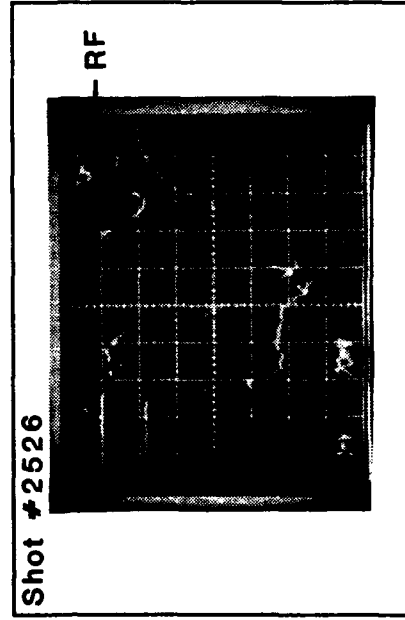
20 ns/div ; 900 W/div

Shot #2453



20 ns/div ; 14 W/div

Shot #2526



20 ns/div ; 700 W/div

Figure 15. Oscilloscope traces of bend exit B-dot RF power vs. time. The low frequency integral of the B-dot is also shown to reference the timing of the RF pulse to the beam arrival. The stellarator gradient was 400 G/cm for a beam current of 325 A and a guide field strength of 1.2 kG in (a), and the beam current was 950 A with a guide field strength of 2.4 kG and a stellarator gradient of (b) 200 G/cm, (c) 250 G/cm, and (d) 400 G/cm.

guide field strength of 2.4 kG and beam current of 950 A, Figures 15(b) through 15(d) show the RF pickup at the bend exit for gradients of, respectively, 200, 250, and 400 G/cm. These data are plotted in Figures 16(a) through 16(d) as logarithmic power versus time to show the growth rates of the unstable mode. The growth rate obtained from these data is twice that for the mode, because it is the power coupled into the B-dot probe that is measured by the square-law detector, rather than the waveguide field amplitude. We have averaged the growth through the exponential rise of the signal, rather than using the faster growth between pauses in the rise of the RF pickup signal. Within the uncertainties of pulse-to-pulse scatter and nonuniform growth within a given pulse, the field growth rates are summarized in Table 2 and compared with those from a recent analysis by T.P. Hughes<sup>[6]</sup> for bounded systems. The average growth time for the 1.2 kG case is more than four times that predicted for the three-wave mechanism, and the 950 A, 2.4 kG growth times are typically 75% longer than the values calculated for the three-wave mechanism. Other frequency components have been observed in RF signals in the experiments, but they are independent of the stellarator gradient. Reversal of the guide field (Larmor and quadrupole rotation in the same sense) eliminates the 2.9 GHz component. With this reversed field orientation, the three-wave interaction is not predicted to produce instability.

Table 2. Power growth times.

Current	$B_s'$	$B_{\text{guide}}$	Growth Time	3-Wave Value
325 A	400 G/cm	1.2 kG	36 ns	8 ns
950 A	200 G/cm	2.4 kG	24 ns	13 ns
950 A	250 G/cm	2.4 kG	18 ns	11 ns
950 A	300 G/cm	2.4 kG	16 ns	9 ns
950 A	400 G/cm	2.4 kG	12 ns	7 ns

The symmetry of the excitation of the B-dot array was investigated by summing the signals from a pair of opposing pickups in a passive "Tee." To minimize the shift in relative

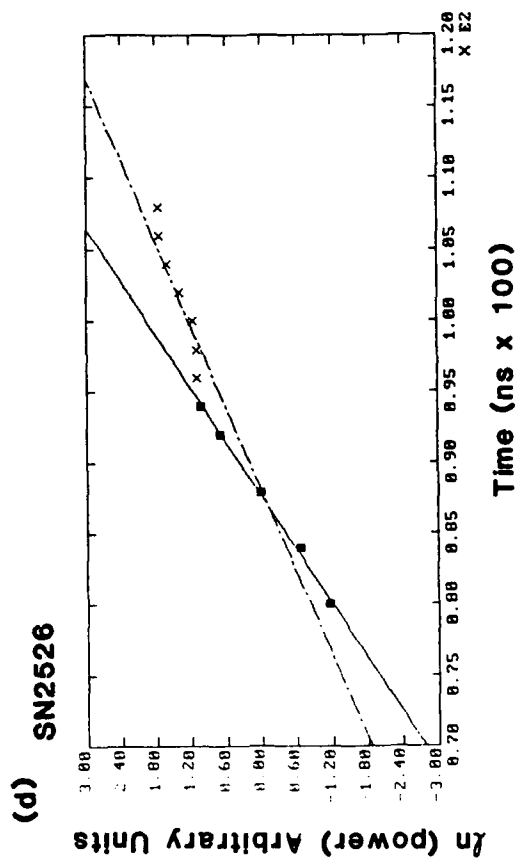
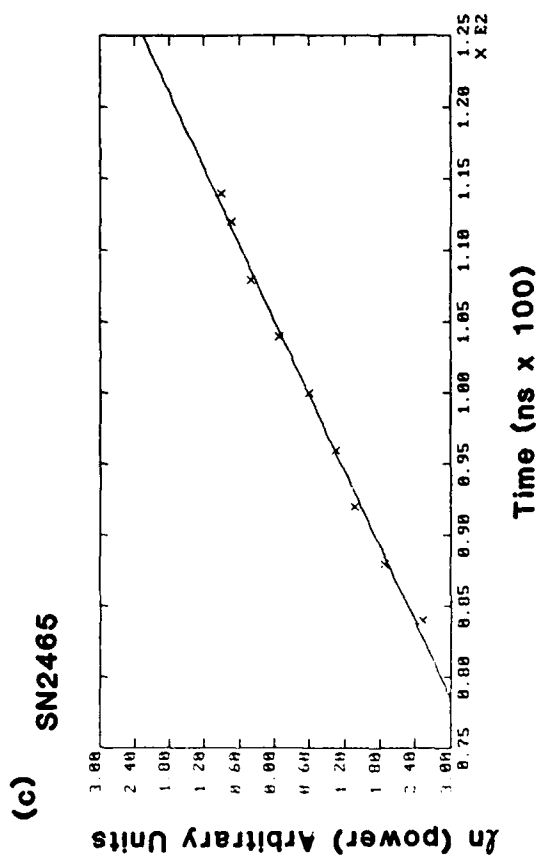
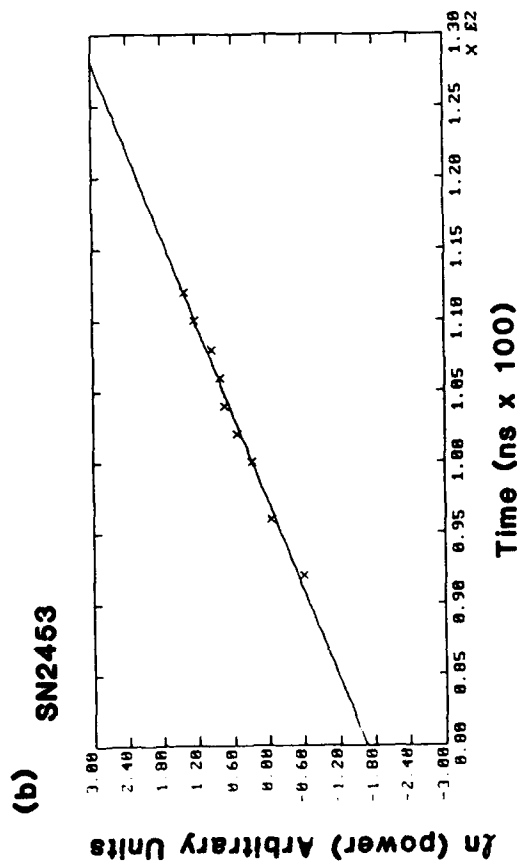
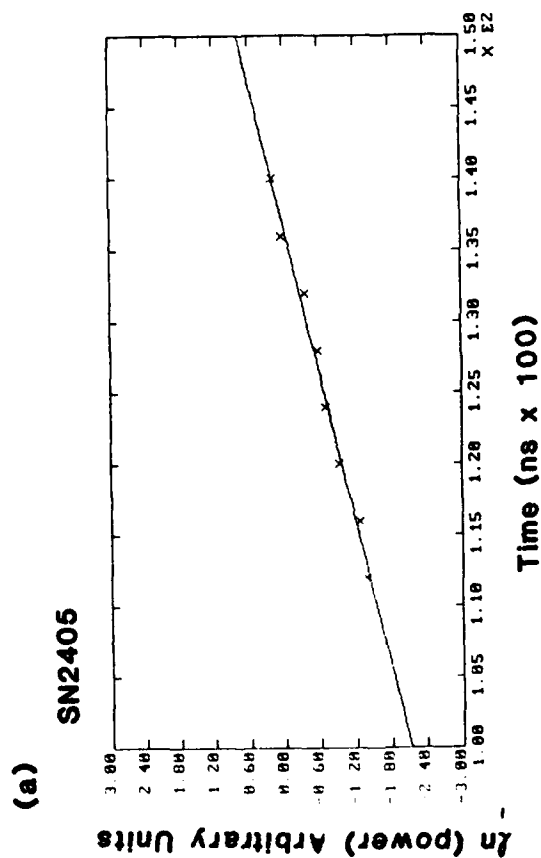


Figure 16. Logarithmic plots of the power vs. time from the data of Figures 15 (a-d), from which some of the growth rate data were derived. The data for 400 G/cm in (d) show a prominent example of a pause in the growth of the RF signal, as seen in most of the other traces, before temporal growth resumes.

phase of the two signals, short cables ( $\sim 5$  ns) of equal length to within about 2 mm ( $\sim 10$  ps) were used to connect the B-dot probes to a Tee (see Figure 17). One 6 dB attenuator was incorporated on each input leg of the Tee to reduce by an additional 12 dB the interference from signals coupled from one B-dot to the other and subsequently reflected back to the Tee. The signal from each leg was measured, terminating both the opposing B-dot and the otherwise open leg of the Tee, and then with both B-dots connected. Finally, a pair of cables with a length difference of 3.2 cm (160 ps) was used to connect the B-dots to the Tee, to provide an approximately 180-degree shift in the relative phase of the 3 GHz components. The results are shown in Figure 18. These traces indicate that the B-dot pickup is largely dipole in character, as would be the case for pickup from a coherent beam oscillation or from the TE<sub>11</sub> waveguide mode. The out-of-phase power is nearly twice that of the individual legs, as would be expected for incoherent pickup, but the in-phase sum power is only 40-50% of the power of either individual leg. These relative powers are consistent with a dominantly dipole excitation with a relative phase shift between the measurements of approximately 100 degrees, rather than the intended 180-degree shift. The low-frequency integral of the sum signal (proportional to the beam current, approximately) is independent of the cable-induced phase shift.

## 9.0 BEAM LOSS

Examples of beam loss are shown in Figure 19 as a function of guide field strength for fixed stellarator gradient and current (300 G/cm and 950 A). The guide field was oriented parallel to the electron velocity and the beam current was measured using the Faraday cup. The data of Figure 20 show beam loss for a fixed guide field and current (2.4 kG and 950 A) as the stellarator gradient increases. Figure 21 shows the Faraday cup response for fixed guide field and stellarator gradient (1.8 kG and 400 G/cm). The beam loss worsens with increasing current and stellarator gradient, but is stabilized by increasing guide field strength. Table 3 shows the width of the central plateau of the Faraday cup traces for various values of the current, guide field, and stellarator gradient. Without loss, the plateau is approximately 80 nsec wide. In some high-gradient, low guide field cases, the

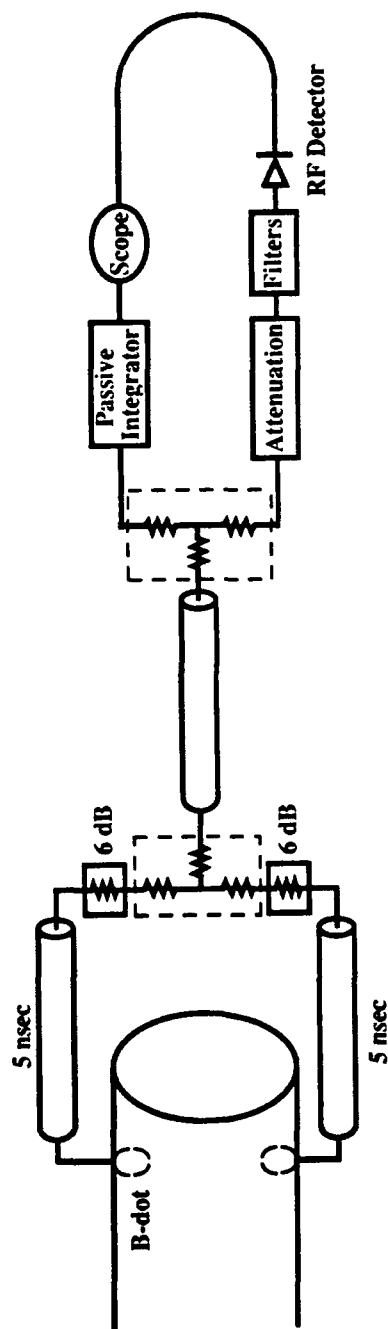
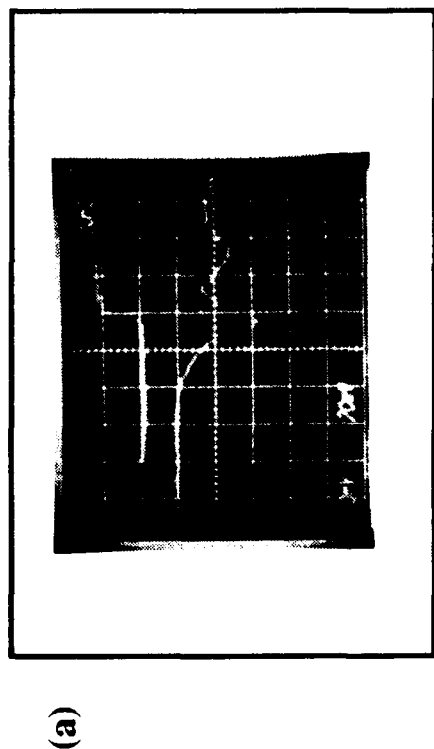
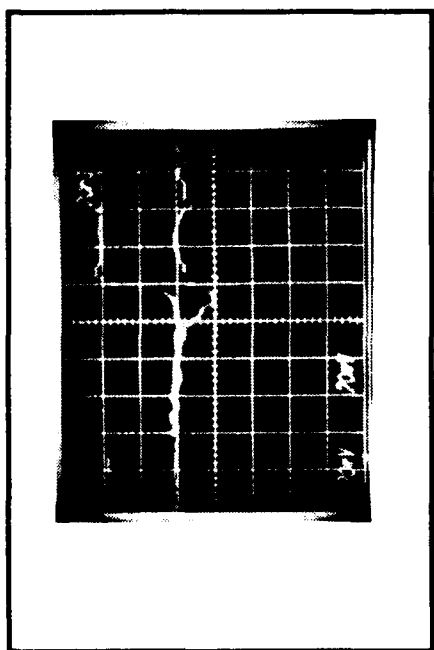


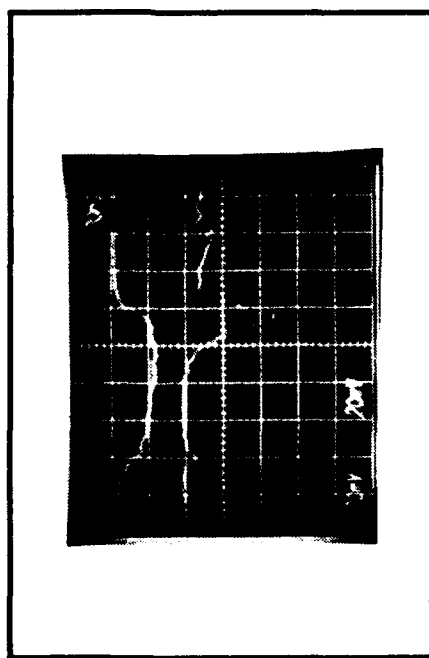
Figure 17. Network used for comparing the sum and difference of opposing B-dots. The 6 db attenuators on each input port of the "Tee" provide additional attenuation of the signal coupled between the B-dots and reflected back to the Tee. Differencing of the  $\sim 3$  GHz signal was done by adding  $\sim 3.2$  cm of length ( $\sim 160$  ps) to one of the 5 ns cables.



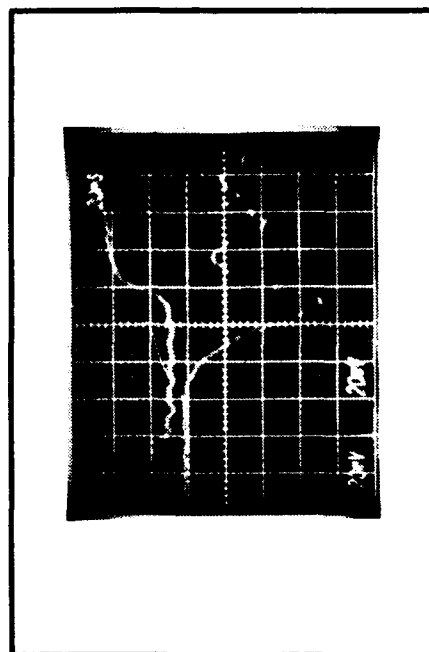
(a)



(c)



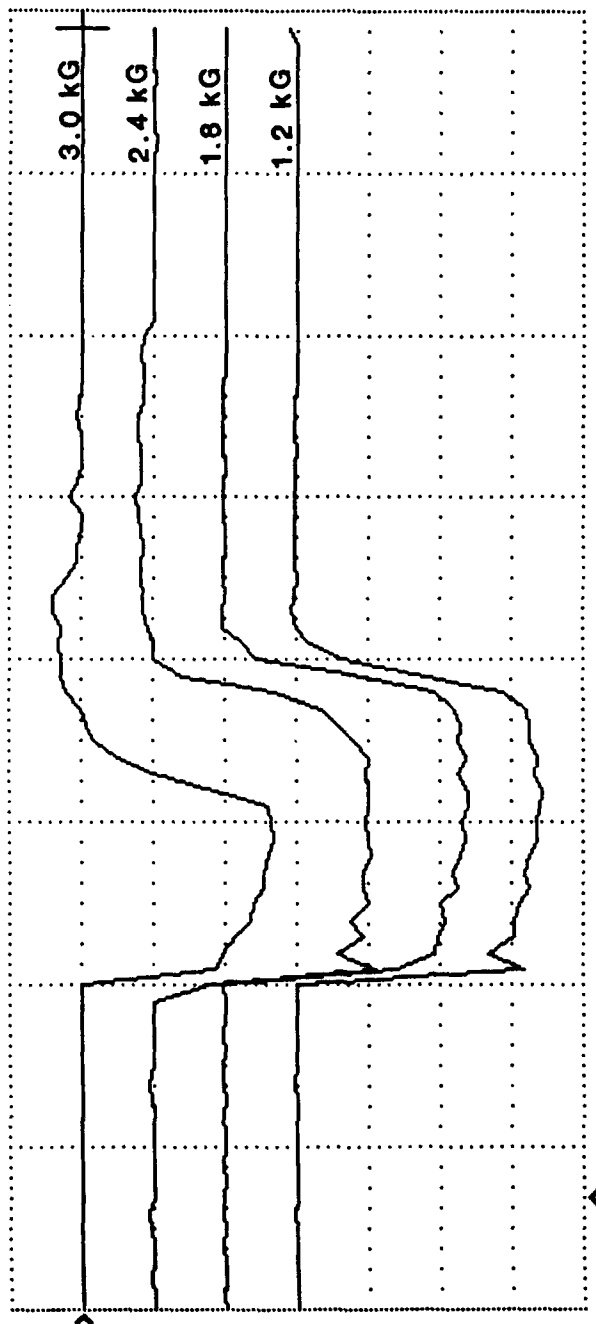
(b)



(d)

Time Base: 20 ns/div ; Vertical Sensitivity: 550 W/div

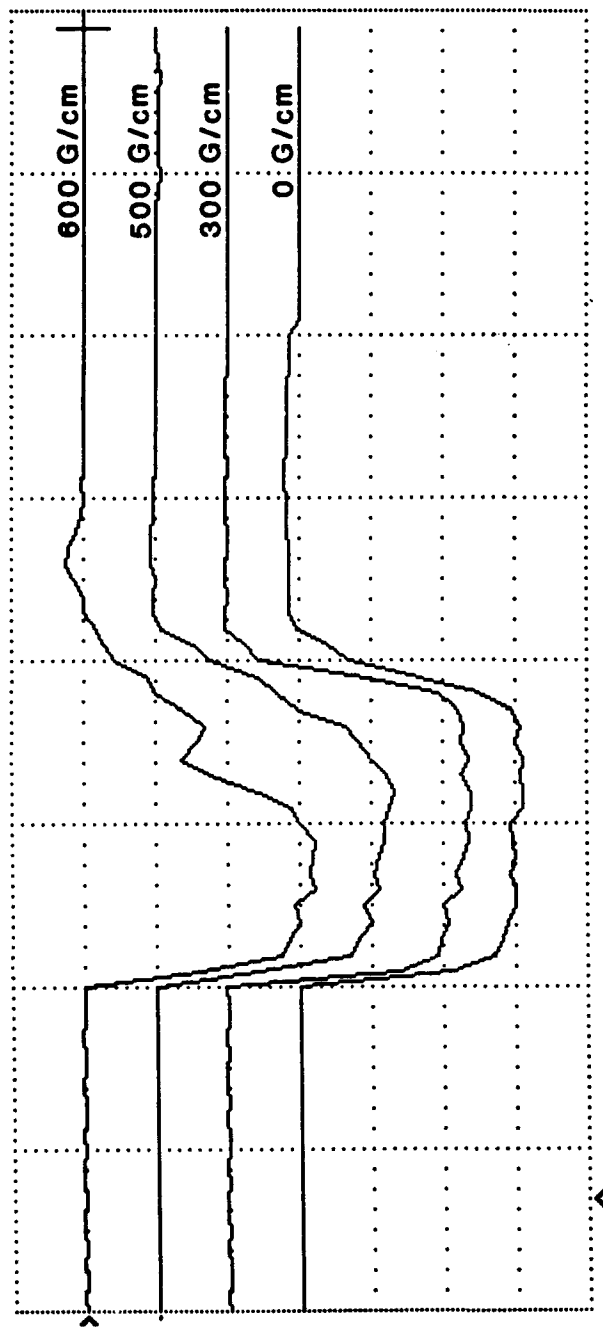
Figure 18. Signals from bend exit B-dots for beam current of 325 A, guide field strength of 1.2 kG, and stellarator gradient of 400 G/cm. (a) Top B-dot probe alone, (b) bottom probe alone, (c) sum of top and bottom with equal cable lengths, and (d) sum of top and bottom probes with cable length differential of 3.2 cm (nominally 160 ps or 170 degrees). Upper trace in all cases is the integrated B-dot signal (arbitrary scale). Lower trace is RF power from diode detector.



Time Base: 50 ns/div ; Vertical Sensitivity: 280 W/div

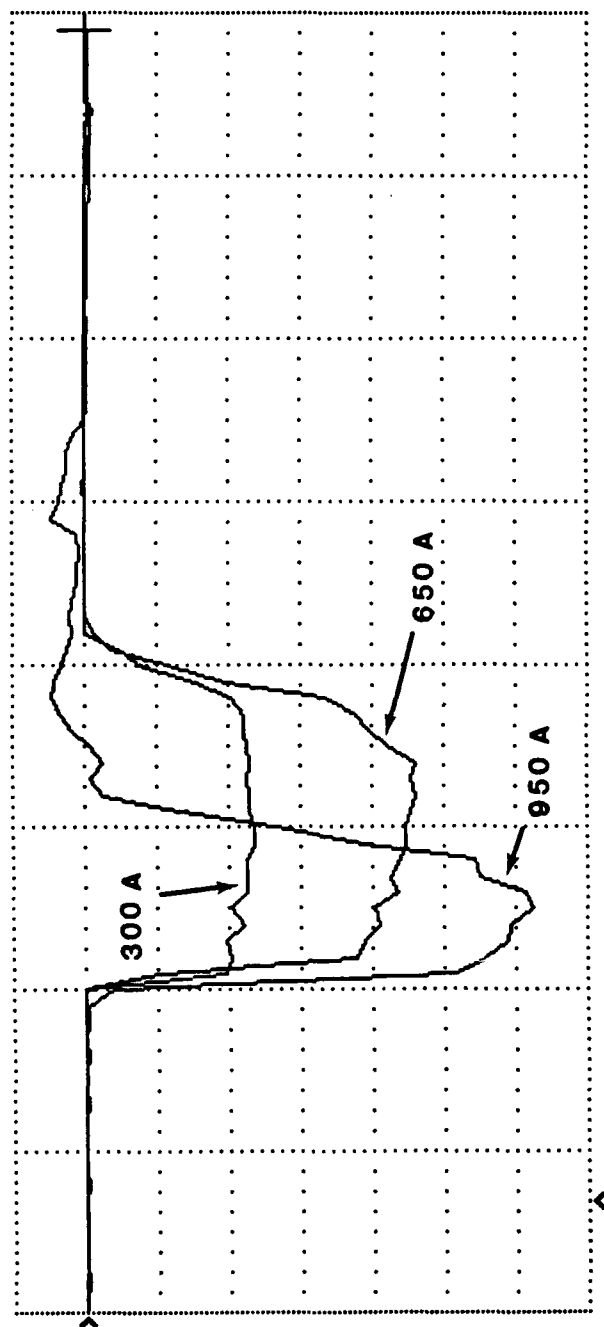
Figure 19. For beam current of 950 A and stellarator gradient of 300 G/cm, beam tail erosion worsens with decreasing guide field strength from bottom to top, respectively, of 1.2, 1.8, 2.4, and 3.0 kG.





Time Base: 50 ns/div ; Vertical Sensitivity: 280 W/div

Figure 20. For 950 A and a guide field strength of 2.4 kG, the beam tail erosion can be seen progressively worsening as the stellarator gradient is raised, from bottom to top, respectively, of 0, 300, 500, and 600 G/cm.



**Time Base: 50 ns/div ; Vertical Sensitivity: 140 W/div**

Figure 21. For a fixed guide field strength of 1.8 kG and stellarator gradient of 400 G/cm, the beam loses progressively more of its tail as the injected current is raised from 325 A, through 650 A, to 950 A. Loss at the tail of the 650 A injected current beam is only visible as a small shoulder in the trailing edge of the beam.

Table 3. Temporal width (ns) of beam pulse passed to Faraday cup for listed values of guide field, stellarator gradient, and peak injected current. Duration of flat-top of current pulse is approximately 80 nsec in the absence of beam loss. In cases for which no part of the pulse flat-top shows full transmission of current, the peak percentage of the nominal injected current is given.

	Stellarator Gradient (G/cm)						
	0	100	200	300	400	500	600
I = 950 A, B <sub>z</sub> (kG):							
1.2	80	80	80	50	35	<40%	<2%
1.8	80	80	80	70	30	50	35
2.4	80	80	80	80	80	50	35
3.0	80	80	80	80	80	80	55
I = 680 A, B <sub>z</sub> (kG):							
1.2	80	80	80	70	45	<50%	<50%
1.8	80	80	80	80	70	55	<80%
2.4	80	80	80	80	80	65	60
3.0	80	80	80	80	80	80	80
I = 325 A, B <sub>z</sub> (kG):							
1.2	80	80	80	80	80	<50%	<50%
1.8	80	80	80	80	80	80	<85%
3.0	80	80	80	80	80	80	80

beam transmission is less than unity across the full pulse width of the beam. In these cases, the peak relative current transmission over the central portion of the beam pulse is given in the table. Orbital and mismatch errors may be at fault, because beam is lost irrespective of the value of the injected current.

## 10.0 SUMMARY

Under the present effort, the performance of the diode and magnetic compression regions has been improved, enabling useful comparison of emittance measurements along the beam channel. These measurements indicate that there is little growth of the emittance of the beam through the straight solenoid and 180-degree bend magnets, to within  $\sim 50\%$  uncertainty in the measurements. Measurements of the offset of the beam at the end of the stellarator channel have validated the theoretical formalism used to calculate the beam dispersion, giving confidence in the methods being used to design future experiments and project the performance that may be reasonably expected for future applications. Measurements of beam loss at the Faraday cup over a wide range of guide field, beam current, and stellarator gradient have indicated the presence of a collective beam instability dependent upon the presence of the stellarator focussing field. Measurements of the RF power coupled out from B-dot probes in the beamline using low- and high-pass filters have shown that the beam is perturbed at a frequency very nearly that of the cutoff of the TE<sub>11</sub> mode in the beamline, and that a waveguide mode at this frequency is left propagating in the beamline after the beam passes. This excitation is absent at low stellarator gradients and low currents, and is present only for electron Larmor motion opposite to the direction of rotation of the stellarator winding. Exponential growth times of the RF excitation were measured as a function of stellarator gradient only for a single value of the beam current (950 A) and a single guide field strength (2.4 kG), and are consistently  $\sim 75\%$  longer than calculated for the instability mechanism of Hughes and Godfrey. The measured growth time for a 325 A beam in a 1.2 kG guide field with a 400 G/cm stellarator gradient was approximately four times as long as expected from the three-wave mechanism. No gain

measurement was made in the present series of experiments, but it is important that this be done in future work.

## 11.0 SUGGESTIONS FOR FUTURE INVESTIGATIONS

It is of interest to develop means of measuring and tuning the particle oscillation frequencies in stellarator beamlines. These techniques should have direct application in the tuning of stellarator fields in accelerator experiments in the near future. Magnetic measurements must be made to determine to what degree the design fields have been implemented in the existing beamline magnets, in order to project what level of magnetic perturbation may be expected in future stellarator beamlines and determine whether fabrication tolerances must be improved to ensure that errors in the particle optics remain tolerable. It is also desirable, for positive identification of the collective beam loss mechanism observed in the experiments, to measure the gain of the interaction, to make growth time measurements over a broad range of guide field strengths, and to alter the waveguide properties of the beamline to determine the frequency dependence of the interaction upon those properties.

## REFERENCES:

- [1] Putnam, S.D., Spiral Line Accelerator, U.S. Patent No. 4,870,368; see also S.D. Putnam, 1987 Part. Accel. Conf., IEEE Cat. No. 87CH2387-9.
- [2] Wilson, M.A.D., 1981 Part. Accel. Conf., IEEE Trans. on Nuc. Sci. NS-28 (3), 3375.
- [3] Roberson, C.W., A. Mondelli, and D. Chernin, Phys. Rev. Lett. 50, 507 (1983).
- [4] Hughes, T.P., and B.B. Godfrey, Phys. Fluids 29, 1698 (1986).
- [5] Curry, R., et al., 6th IEEE Pulsed Power Conference, Arlington, Va., 1987; IEEE Cat. No. 87CH2522-1, p. 248.
- [6] T.P. Hughes, private communication.